Department of Structural Engineering
Faculty of Engineering Science and Technology
NTNU- Norwegian University of Science and Technology

ACCESSIBILITY

OPEN

MASTER THESIS 2011

SUBJECT AREA:	DATE:	NO. OF PAGES:
POLYMER ENGINEERING	14 JUNE 2011	102+33

TITLE:

Plastic deformation and fracture of polymer materials

Plastisk deformasjon og brudd i polymerer

BY:

Anfrid Dahlen

SUMMARY:

Polymer materials are known to dilate during plastic deformation. This thesis is a study on some of the mechanisms behind the volume change and how it is affected by triaxiality in stress. The goal was to assess how the current hyperelastic-viscoplastic constitutive material model for thermoplastics made at Structural Impact Laboratory (SIMLab) could be developed further.

The volume change was studied by conducting tension tests on axisymmetric smooth and notched specimens made of high-density polyethylene (HDPE) and polyvinyl chloride (PVC). In order to change the stress triaxiality, the notched specimens had four different notch radii. All tests were monitored by a digital charge-coupled device (CCD) camera. To map the deformations of the specimens, the images were post processed in a custom-made digital image correlation (DIC) algorithm that was created in the numerical computing environment and programming language MATLAB. Further, simulations of the tests were run in the finite element software LS-DYNA, using the implemented material model for thermoplastics developed at SIMLab. SIMLab's material model is currently based on the Raghava yield surface and plastic potential. A modification of the model, employing the Gurson - Tvergaard - Needleman (GTN) yield surface and plastic potential incorporating the evolution of voids during deformation of the material, was also evaluated.

A relationship between the stress triaxiality and the volume strain during plastic deformations was found from the tests. The stress triaxiality was also found to affect the yield stress, the local strain rate, the radial strain, the equivalent plastic fracture strain and the fracture surface. The tests also suggest that nucleation of voids should be described as strain controlled. Comparing the tests to the simulations it was evident that the volume change in the materials was not captured properly with the model employing the Raghava potential. The simulations using the GTN potential however, showed far better estimations of the volume strain. Adjustments of the model employing the GTN yield surface and plastic potential are still required to simulate the strain softening properly.

RESPONSIBLE TEACHER: Professor Arild H. Clausen

SUPERVISORS: PhD Student Anne Serine Ognedal, Professor Odd Sture Hopperstad

CARRIED OUT AT: SIMLab, Department of Structural Engineering, NTNU

NORGES TEKNISK-NATURVITENSKAPELIGE UNIVERSITET
INSTITUTT FOR KONSTRUKSJONSTEKNIKK

MASTER THESIS 2011

Anfrid Dahlen

Plastic deformation and fracture of polymer materials

(Plastisk deformasjon og brudd i polymerer)

Polymers are in many ways more challenging than other types of materials: They can be very ductile, viscous effects are important (temperature and strain rate sensitivity), different responses are observed in tension and compression etc. During the last couple of years, a new constitutive model for polymer materials has been developed at SIMLab. This model has been proved to be well-suited to describe different stress states for large deformations. Unlike metals, polymers may change volume during plastic deformation. This volume change is often related to damage, i.e. voids and microcracks occurring in the material. One drawback with the material model is that it does not capture volume change, and also not the damage, correctly. A next step in the development of the model is to include the damage evolution. Our long term goal is to define a ductile fracture criterion. In order to do this, we need to investigate the mechanisms behind the volume change.

As a part of this work it is valuable to gain some information of how the volume change is affected by the stress triaxiality. In physical tests, the triaxiality can be changed by applying notched samples with different notch radii.

First we will learn about the polymers' mechanical properties, then we will look at the material model. The master candidate will do experimental tests on notched circular tensile test samples of PVC and HDPE and study how the volume is changing with stress state. The experiments should be compared with numerical results from LS-DYNA analysis.

Some keywords for activities related to this master thesis project are:

- Literature: Polymers in general and the material model. Notched tension samples.
- Experimental tests: Tension test samples with different notch radii. Presentation of test results.
- Numerical modelling: Simulation of experimental tests. Comparison with experimental results.

The candidate may agree with the supervisors to pay particular attention to specific parts of the investigation, or include other aspects than those already mentioned.

The thesis is to be organized as a research report, recognising the guidelines provided by Department of Structural Engineering.

Supervisors: Anne Serine Ognedal, Arild H. Clausen, Odd Sture Hopperstad

The report is to be handed in at Department of Structural Engineering not later than 14 June 2011.

NTNU, 17 January 2011
Arild H. Clausen
Professor

Acknowledgements

I would like to thank PhD student Anne Serine Ognedal for her catching commitment, and for always taking the time to give guidance. Also, I would like to express my gratitude to Professor Arild H. Clausen for sharing his great knowledge both when it comes to polymers and writing a master thesis, and to Professor Odd Sture Hopperstad for thinking clever thoughts and helping with the interpretation of the test and simulation results. I am also sincerely grateful for Virgile Delhaye letting me try his modified material model that is under development, and for helping with the calibration of the model.

I would also like to thank Chief Engineer Trond Auestad for patient guidance in the laboratory, PhD student Egil Fagerholt for finding the least squares in MATLAB and Research Scientist Torodd Berstad for great help with the simulations in LS-DYNA.

Also, a thank you is directed towards my fellow students for showing great team spirits, both on and off campus.

Trondheim, 14th of June 2011

Anfrid Dahlen

Table of Contents

Acronyms

CCD	charge-coupled device
CPU	central processing unit
DIC	digital image correlation
GTN	Gurson - Tvergaard - Needleman
HDPE	high-density polyethylene
PE	polyethylene
PVC	polyvinyl chloride
SIMLab	Structural Impact Laboratory
SLR	single-lens reflex

List of Figures

1 Introduction

Polymers are cheap, easy to form, light, ductile and - depending on the additives and environment - sustainable. Because of these characteristics the demand for polymers has increased significantly for the last decade; their use is widely spread in the production of structural and safety parts for automobiles, and because of their outstanding energy absorption abilities they are becoming adopted into fields where other materials - such as metals - earlier were the common choice.

Numerical simulations are an important part in the design of load carrying components today. As the use of polymers has increased, so has the desire for running precise numerical simulations for these materials. The need for a reliable constitutive material model for polymers is therefore of an increasing importance. Material models for elastomers and thermosets are already rather well defined, but for thermoplastics there is still need for improvements according to Bois et al. [2005].

At the Structural Impact Laboratory (SIMLab), a centre for research-based innovation at the Department of Structural Engineering at NTNU, a hyperelastic-viscoplastic constitutive material model for thermoplastics has been under development for the last few years. The project was initiated at the request of SIMLabs industrial partners, such as Statoil, Audi and Renault, who wanted an improvement of the existing thermoplastic models. The SIMLab

developed model now describes different stress states for large deformations in a satisfying way, but - it does not include the evolution of damage. Polymers are - in opposition to metals - compressible, and may therefore change volume during plastic deformation. The volume change is often related to damage, i.e. voids and microcracks occurring in the material.

The objective of this thesis was to study how the plastic dilation in polymer material is affected by triaxiality in stress. The plastic dilation were studied through tensile tests and numerical simulations of axisymmetric smooth and notched specimens made of the thermoplastics high-density polyethylene (HDPE) and polyvinyl chloride (PVC). The notched specimens had four different notch radii, in order to obtain different triaxial stress states.

To map the stress and strain fields of such specimens are a demanding task. Techniques similar to the one described by Hovden [2010] and Kamaya and Kawakuboa [2011] has been performed several times at e.g. SIMLab; introducing small black dots on the surface of a specimen and mapping the deformation of the specimen using digital image correlation (DIC) software, such as 7D, to compare images acquired with a charge-coupled device (CCD) camera during the test. Using such techniques have however failed due to the large displacements over relatively small areas and difficulties with a low depth of focus. To overcome these problems, a custom made DIC algorithm capturing the displacement of given points as well as the curvature of the root of the notch was created for the post-processing of the tests.

The report starts by describing the background theory for the work executed in this thesis in Chapter 2. Further, in Chapter 3, the laboratory tests are described, and basic results from the tests are presented. The numerical simulations performed in LS-DYNA using the current material model are presented in Chapter 4, and in Chapter 5 the results of the tests and simulations are compared. In Chapter 6 simulations in LS-DYNA with a modified version of the material model is presented, and in Chapter 7 fractures and fracture surfaces from the tests are examined. Last, in Chapter 8, conclusions and recommendations for further work are presented.

2

Theoretical Background

In order to interpret the experimental work and numerical simulations presented later in the thesis, some background knowledge is required. In the following chapter polymer materials are described, and a material model for thermoplastics is introduced. Stress triaxiality is defined and prediction of fractures and fracture surface topology are discussed.

2.1 Polymer Materials

The term Polymers stems from Greek and means many parts [Ram, 1997], aiming to describe a molecule composed of many identical units. These identical units are called monomers. Numerous monomers together forms macromolecules, often as large molecular chains held together by covalent bonds between the atoms. In one chain there are typically 10^3 to 10^5 monomers, which gives a molecular length of up to a few micrometers [Rösler et al., 2007].

These molecular chains are also bonded to each other, but usually by much weaker bonds such as van der Waals, dipole, or hydrogen bonds. However, there can also be covalent bonds between the chains. Such cross-links creates a molecular network by fixing the chains relative to each other. Based on this knowledge, polymers can be divided into three different types: Thermoplastics, elastomers and duromers (see Figure 2.1). A thermoplastic

has no cross-linkage. Elastomers - also called rubbers - has a small number of cross-links, about 1 cross-link per 1000 atoms of the main molecule chain. Duromers - also called thermosetting polymers, thermosets or resins - has many cross-links, may be as many as 1 for every 20 atom in the main molecule chain. Thermosets are therefore much stiffer than elastomers [Rösler et al., 2007, Polanco-Loria et al., 2010].

(a) Thermoplastic (b) Elastomer (c) Duromer

Figure 2.1: Schematic Sketch of the Cross-linking of Different Polymers [Rösler et al., 2007]

The cross-linking between the molecular chains is very important when deciding the mechanical properties of a polymer - when cross-links fix chains relative to each other, it can make it impossible to draw out single molecules. In addition, the length of the molecules - which is proportional to the relative molecular mass - also affects the mechanical properties of a polymer [McCrum et al., 1997].

A region with regular arrangement of the molecular chains is called a crystalline region. If there are no regular arrangements the region is called amorphous. The volume fraction of crystalline regions compared to the volume fraction of amorphous ones is termed as the crystallinity of the material. Cross-links make it impossible for elastomers and duromers to have a regular arrangement of the chain molecules, and thus they will always be completely amorphous. Thermoplastics, which has no cross linkage, can contain both amorphous and crystalline regions, i.e. be semi-crystalline.

It is generally not possible for polymers to be fully crystalline. In theory, the chain molecules could form a parallel, regular structure, but because of their length this is not very likely. Usually a chain molecule will be twisted and entangled with other molecules, and a polymers structure is therefore always at least partially amorphous [Rösler et al., 2007].

2.2 Material Model

Thermoplastics occupies certain characteristics, and a material model for thermoplastics should allow for these. First of all, when thermoplastics deforms it involves large elastic and plastic deformations. They often have a higher yield strength in compression than in tension [Raghava et al., 1973], and their mechanical response is often temperature and strain rate sensitive [Arruda et al., 1995, Dupaix and Boyce, 2007]. Volume change during plastic deformation has also been observed [Delhaye, 2010]. And, after the yield limit, some polymers show a stress softening behaviour, while others show monotonic hardening [G'Sell et al., 1992].

SIMLab has developed a hyperelastic-viscoplastic constitutive material model for thermoplastics [Polanco-Loria et al., 2010]. The developed material model is a modification of a model that was proposed by Boyce et al. [2000]. The model is assumed to consist of two parts, A and B, representing the two basic resistances to deformation. Part A represents the hyperelastic-viscoplastic resistance related to intermolecular strength; i.e. the forces acting between the molecular chains. Part B is an entropic resistance evolving due to molecular orientation; the entropy is reduced as the molecular chains are stretched. Both parts have the same deformation gradient $\mathbf{F} = \mathbf{F}_A = \mathbf{F}_B$, and thus the same volume change J, since $J = det(\mathbf{F})$. The true stress $\boldsymbol{\sigma}$ is the sum of the contributions from each part, $\boldsymbol{\sigma} = \boldsymbol{\sigma}_A + \boldsymbol{\sigma}_B$.

In Figure 2.2, the main constituents of the model are summarised. A conceptual illustration of the kinematics of the model is shown in Figure 2.3. Ω_0 represents the reference configuration, $\bar{\Omega}_A$ the intermediate configuration

and Ω the current configuration. $\mathbf{F}_A^e$ is the elastic part of $\mathbf{F}_A$ and $\mathbf{F}_A^p$ is the plastic part, $J_A = det(\mathbf{F}_A^e \mathbf{F}_A^p)$. The model does not include thermal effects.

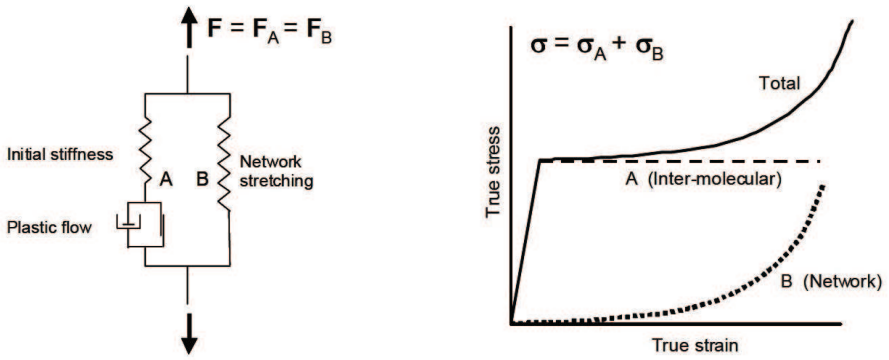

(a) Principle of Material Model (b) Uniaxial Stress - Strain Relationship

Figure 2.2: Proposed Constitutive Model [Polanco-Loria et al., 2010]

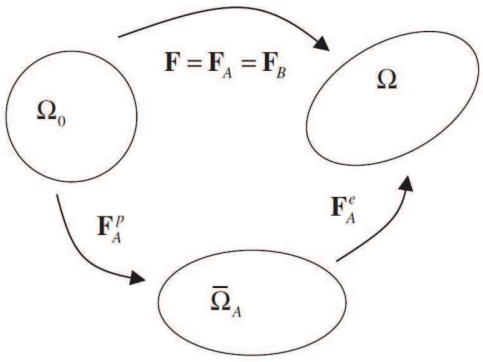

Figure 2.3: Kinematics of the Model [Polanco-Loria et al., 2010]

2.2.1 Inter-molecular resistance (Part A)

It is assumed that the elastic part of the deformation follows the compressible Neo-Hookean material model, which is an extended version of Hooke's law for large elastic deformations. The Kirchhoff stress $\boldsymbol{\tau}_A$ on $\bar{\Omega}_A$ gives the elastic constitutive law [Polanco-Loria et al., 2010]

$$\boldsymbol{\tau}_A = \lambda_0 ln(J_A^e)\mathbf{I} + \mu_0[\mathbf{B}_A^e - \mathbf{I}] \tag{2.1}$$

where J_A is the Jacobian of Part A, $J_A = det(\mathbf{F}_A)$, representing the volume change, and can be decomposed in a plastic and an elastic part by a multiplicative split as $J_A = det(\mathbf{F}_A^e \mathbf{F}_A^p) = J_A^e J_A^p$. Further $\mathbf{B}_A^e = \mathbf{F}_A^e \cdot (\mathbf{F}_A^e)^T$ is the elastic left Cauchy-Green deformation tensor, and $\mathbf{I}$ represents the second order unit tensor. It is assumed that the intermediate configuration $\bar{\Omega}_A$, defined by $\mathbf{F}_A^p$, is invariant to rigid body rotations of the current configuration.

λ_0 and μ_0 represents the classical Lamé constants of the linearised theory - and are, according to the classical theory of elasticity, related to Young's Modulus E_0 and Poisson's ratio ν_0 by

$$E = \frac{\mu_0(3\lambda_0 + 2\mu_0)}{\lambda_0 + \mu_0} \tag{2.2}$$

$$\nu = \frac{\lambda_0}{1(\lambda_0 + \mu_0)} \tag{2.3}$$

Between the Kirchhoff stress $\boldsymbol{\tau}_A$ and the Cauchy stress $\boldsymbol{\sigma}_A$ on $\bar{\Omega}_A$ there exist a relationship defined as [Belytschko et al., 2000]

$$\boldsymbol{\tau}_A = J_A^e \boldsymbol{\sigma}_A \tag{2.4}$$

The current material model uses the Raghava yield criterion and plastic potential. The Gurson - Tvergaard - Needleman (GTN) yield criterion and plastic potential has also been proposed as suitable by Delhaye [2010], to modify the material model to account for macroscopic damage owing to growth of cavities in a material. Both yield criterions and plastic potentials are therefore presented next.

Raghava Yield Criterion and Plastic Potential

As the von Mises criterion is based on the deviatoric stress component only, the Raghava criterion [Raghava et al., 1973] takes the hydrostatic stress component into account. The latter also accommodates differences for the yield stress in tension and compression.

The Raghava criterion can be stated as

$$(\sigma_1-\sigma_2)^2+(\sigma_2-\sigma_3)^2+(\sigma_3-\sigma_1)^2+2(|\sigma_C|-|\sigma_T|)(\sigma_1+\sigma_2+\sigma_3) = 2|\sigma_C\sigma_T| \quad (2.5)$$

where σ_1, σ_2 and σ_3 denotes the principal stresses of the applied stress state. σ_C is the compressive yield strength, and σ_T the tensile yield strength. Thus, for σ_C and σ_T being equal, Equation (2.5) will be reduced to the von Mises criterion.

By using the first invariant of the stress tensor I_1, the influence of the hydrostatic portion of the applied stress state is introduced. Further, $\alpha = \sigma_C/\sigma_T \geq 1$ is introduced as the yield stress ratio, describing pressure sensitivity. The yield surfaces for the Von Mises criterion and the Raghava criterion with $\alpha = 1.3$ are shown in Figure 2.4.

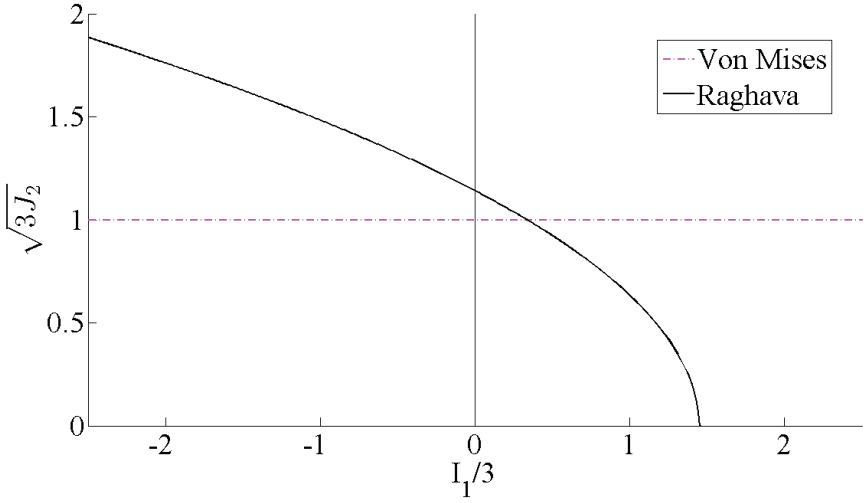

Figure 2.4: Yield Surfaces

Yielding occurs when the yield criterion $f_A = \bar{\sigma}_A - \sigma_T = 0$ is satisfied. The equivalent stress $\bar{\sigma_A}$ is defined as [Raghava et al., 1973]

$$\bar{\sigma_A} = \frac{(\alpha - 1)I_{1A} + \sqrt{(\alpha - 1)^2 I_{1A}^2 + 12\alpha J_{2A}}}{2\alpha} \tag{2.6}$$

J_2 is here the deviatoric stress invariant.

When choosing a flow rule for Part A, an associated flow cannot be used - as it predicts unrealistic large volumetric plastic strains [Polanco-Loria et al., 2010]. A non-associative flow rule should therefore rather be used, to ensure control over the plastic dilatation. The Raghava-like plastic potentials flow rule can be written as

$$g_A(I_{1A}, J_{2A}) = \frac{(\beta - 1)I_{1A} + \sqrt{(\beta - 1)^2 I_{1A}^2 + 12\beta J_{2A}}}{2\beta} \geq 0 \tag{2.7}$$

where $\beta \geq 1$ is a parameter controlling the volumetric plastic strain.

From the flow rule, the plastic rate-of-deformation tensor is $\mathbf{D}_A^p = \dot{\bar{\epsilon}}_A^p \partial g_A / \partial \boldsymbol{\sigma}_A$. The equivalent plastic strain rate is chosen as Polanco-Loria et al. [2010]

$$\dot{\bar{\epsilon}}_A^p = \left\{ \begin{array}{rl} 0 \quad \text{if} & f_A \leq 0 \\ \dot{\epsilon}_{0A} \left\{ \exp\left[\frac{1}{C} \left(\frac{\bar{\sigma}_A}{\sigma_T} - 1 \right) \right] - 1 \right\} \quad \text{if} & f_A > 0 \end{array} \right\} \tag{2.8}$$

C and $\dot{\epsilon}_{0A}$ can easily be found from uniaxial strain-rate tests.

Gurson - Tvergaard - Needleman Yield Criterion and plastic potential

The GTN model was originally a theory of dilatational plasticity developed by Gurson [1977], which was later modified by Tvergaard and Needleman [1983] to make the model correspond better with their numerical studies. The model takes into account the dependency of the yield stress upon hydrostatic stress and incorporates damage owing to growth of cavities[Lemaitre and

Desmorat, 2005]. Cavity growth is included in the function by introducing the volume fraction of voids f as a damage variable.

To model yielding and plastic flow, an elastic-viscoplastic framework is used. Thus, yield will occur when a certain yield criterion Y_A is satisfied

$$Y_A = \bar{\sigma}_A - \sigma_Y = 0 \tag{2.9}$$

where $\bar{\sigma}_A$ is an equivalent stress and σ_Y is a yield stress. A formula for the yield criterion can then be written as [Delhaye, 2010]

$$Y_A = \left(\frac{\sigma_e}{\sigma_{matr}}\right)^2 + 2\Lambda_Y cosh\left(\frac{qI_{1A}}{2\sigma_{matr}}\right) - (1 + \Lambda_Y^2) = 0 \tag{2.10}$$

here, σ_e is the equivalent von Mises stress and σ_{matr} is the yield stress of the matrix material of the cell, which is assumed to increase with the straining of the material. Λ_Y is assumed to be a rational function of f, similarly as suggested by Pijnenburg and Van der Giessen [2001]. Λ_Y accounts for f affecting the size of filaments formed between voids in the matrix, and is by Delhaye [2010] assumed as

$$\Lambda_Y = f^h \tag{2.11}$$

where $h > 0$ is a parameter depending on the matrix properties. Further, q is a parameter that is introduced analogous to Tvergaard and Needleman [1983], and $I_{1A} = tr(\bar{\Sigma}_A)$ is the first invariant of the Mandel stress tensor $\bar{\Sigma}_A$. Since $\bar{\Sigma}_A$ is symmetric, due to the assumption of isotropic elasticity, I_{1A} can also be found using the Kirchhoff stress tensor τ_A, $I_{1A} = tr(\tau_A)$.

Since both $\bar{\sigma}_A \geq 0$ and $\sigma_Y \geq 0$, the yield criterion can be formulated as $Y_A = \bar{\sigma}_A^2 - \sigma_Y^2 = 0$. Equation (2.10) can then be rewritten as

$$\bar{\sigma}_A = \sigma_e \tag{2.12}$$

$$\sigma_Y = \sigma_{matr}\sqrt{1 + \Lambda_Y^2 - 2\Lambda_Y cosh\left(\frac{qI_{1A}}{2\sigma_{matr}}\right)} \tag{2.13}$$

σ_Y is now decomposed into two contributions, after Equation (2.13). A matrix contribution, σ_{matr}, and a square root factor accounting for the void growth effect. If the material is unvoided, i.e. $f = 0$, σ_Y will equal σ_{matr}, which is logical.

To account for the effect of the onset of plastic flow depending on the state of stress, it is assumed that the matrix is pressure dependent as

$$\sigma_{matr} = \sigma_0 + \varphi p \tag{2.14}$$

where σ_0 represents the shear strength of the matrix, analogous as suggested by Pijnenburg and Van der Giessen [2001]. φ is an adjustment parameter and p is the pressure given as

$$p = -\frac{1}{3}tr(\boldsymbol{\tau}_A) = -\frac{1}{3}tr(\bar{\boldsymbol{\Sigma}}_A) \tag{2.15}$$

The parameters describing the pressure dependency of the material φ and σ_0, can be calculated using the yield stress in compression and in tension at the reference strain rate. Using the yield criterion in Equation (2.13) leads to [Delhaye, 2010]

$$\sigma_T = \left(\sigma_0 - \frac{\varphi}{3}\sigma_T\right)\sqrt{1 + \Lambda_Y^2 - 2\Lambda_Y cosh\left(\frac{q\sigma_T}{2(\sigma_0 - \frac{\varphi}{3}\sigma_T)}\right)} \tag{2.16}$$

$$\sigma_C = \left(\sigma_0 + \frac{\varphi}{3}\sigma_C\right)\sqrt{1 + \Lambda_Y^2 - 2\Lambda_Y cosh\left(\frac{q\sigma_C}{2(\sigma_0 + \frac{\varphi}{3}\sigma_C)}\right)} \tag{2.17}$$

To determine φ and σ_0, the set of Equations (2.16) and (2.17) can be solved numerically or graphically.

The flow rule is defined on the intermediate configuration $\bar{\Omega}_A$, and predicts the evolution of the plastic flow as

$$\bar{\mathbf{L}}_A^p = \dot{\bar{\epsilon}}_A^p \bar{\mathbf{r}}_A \,, \quad \bar{\mathbf{r}}_A = \frac{\partial \Phi_A}{\partial \bar{\boldsymbol{\Sigma}}_A} \tag{2.18}$$

here, $\dot{\bar{\epsilon}}_A^p$ is a viscoplastic multiplier, and gives the flow amplitude. $\bar{r}_A$ is a gradient defining the direction of the flow of the plastic potential Φ_A.

Further, the plastic potential is defined as [Delhaye, 2010]

$$\Phi_A = \frac{\sigma_e^2}{\sigma_0^2} + 2\Lambda_\Phi \cosh\left(\frac{qI1A}{2\sigma_0}\right) - (1 + \Lambda_\Phi^2) \tag{2.19}$$

where

$$\Lambda_\Phi = f^g \,, \quad g \geq 0 \tag{2.20}$$

The definition in Equation (2.19) is based on a non-associated theory to predict the plastic flow in a more realistic way, and especially to predict the volume changes related to the evolution of cavities.

According to Polanco-Loria et al. [2010], the viscoplastic multiplier $\dot{\bar{\epsilon}}_A^p$ can be found from

$$\dot{\bar{\epsilon}}_A^p = \left\{ \begin{array}{rl} 0 \quad \text{if} \quad Y_A \leq 0 \\ \dot{\epsilon}_{0A} \left\{ \exp\left[\frac{1}{C} \left(\frac{\bar{\sigma}_A}{\sigma_Y} - 1 \right) \right] - 1 \right\} \quad \text{if} \quad Y_A > 0 \end{array} \right\} \tag{2.21}$$

where the coefficients $\dot{\epsilon}_{0A}$ and C easily can be determined from strain-rate tests.

The GTN model has gained popularity when it comes to simulating plastic flow localization and ductile fracture due to its ability to incorporate the explicit softening processes, such as the softening that arises from microvoid nucleation and growth [Zhang and Niemi, 1995]. The change of the microvoid volume fraction can, according to Belytschko et al. [2000], be written as

$$\dot{f} = \dot{f}_{growth} + \dot{f}_{nucleation} \tag{2.22}$$

where $\dot{f}_{growth}$ represents the growth of existing microvoids and $\dot{f}_{nucleation}$ the nucleation of new microvoids. It is assumed that $f_{nucleation}$ is negligible because the materials considered contain a great deal of particles. Thus

$$\dot{f} = \dot{f}_{growth} \tag{2.23}$$

Using the condition that the matrix material is plastically incompressible, the growth of existing microvoids can be determined from the equation of mass conservation as [Delhaye, 2010]

$$\dot{f}_{growth} = \dot{\bar{\epsilon}}^p_A (1 - f) tr(\bar{\mathbf{r}}_A) \tag{2.24}$$

To use the evolution law in Equation (2.24), the void density of the undeformed material f_0, is needed.

Since the elastic parameters E and ν changes with the density of voids, they have to be corrected during the calculations. They can be corrected by [Steenbrink and Van der Giessen, 1999]

$$E = \frac{2E_0(7 - 5\nu_0)(1 - f)}{2(7 - 5\nu_0) + (1 + \nu_0)(13 - 15\nu_0)f} \tag{2.25}$$

$$\nu = \frac{2\nu_0(7 - 5\nu_0) + (1 + \nu_0)(3 - 5\nu_0)f}{2(7 - 5\nu_0) + (1 + \nu_0)(13 - 15\nu_0)f} \tag{2.26}$$

where E_0 and ν_0 are Young's modulus and Poisson's ratio of the matrix material, respectively.

2.2.2 Network resistance (Part B)

The intra-molecular forces are assumed to follow Anand's constitutive model for compressible elastomeric solids [Anand, 1996]. The resistance of the

polymer network is assumed to be hyperelastic and the network orientation is represented by the deformation gradient $\mathbf{F}_B$. The elastic constitutive law in terms of the Kirchhoff stress $\boldsymbol{\tau}_B = J_B \cdot \boldsymbol{\sigma}_B$ on Ω is given by the following [Polanco-Loria et al., 2010]

$$\boldsymbol{\tau}_B = \frac{C_R}{3}\frac{\overline{\lambda}_L}{\overline{\lambda}}\mathcal{L}^{-1}\left(\frac{\overline{\lambda}}{\overline{\lambda}_L}\right)(\mathbf{B}_B^* - \overline{\lambda}^2\mathbf{I}) + \kappa(lnJ)\mathbf{I} \tag{2.27}$$

where $J_B = det(\mathbf{F}_B)$, identical as for Part A. $\mathcal{L}^{-1}$ is the inverse of the Langevin function

$$\mathcal{L}(\chi) = \coth\chi - 1/\chi \tag{2.28}$$

and $\overline{\lambda}$ is the effective distortional stretch given as

$$\overline{\lambda} = \sqrt{\frac{1}{3}tr(\mathbf{B}_B^*)} \tag{2.29}$$

where, $\mathbf{B}_B^* = \mathbf{F}_B^* \cdot (\mathbf{F}_B^*)^T$ is the distortional left Cauchy-Green deformation tensor. $\mathbf{F}_B^* = J_B^{-1/3}\mathbf{F}_B$ is the distortional part of $\mathbf{F}_B$.

2.2.3 Summary of Material Model Parameters

The required input parameters for the two parts of the current material model is presented in Table 2.1 and 2.3 [Polanco-Loria et al., 2010]. The input parameters needed for Part A if using the GTN yield surface and plastic potential is presented in Table 2.2 [Delhaye, 2010].

Table 2.1: Parameters Part A (Raghava)

$\dot{\epsilon_{0A}}$	Reference strain rate
C	Magnitude of strain rate dependency
E	Young's Modulus
ν	Poisson's Ratio
σ_T	Yield stress in uniaxial tension
α	Yield stress ratio in uniaxial loading
σ_s	Saturation stress
H	Ramping parameter of stress between σ_T and σ_s
β	Dilatation parameter in plastic potential function

Table 2.2: Parameters Part A (GTN)

$\dot{\epsilon}_{0A}$	Reference strain rate
C	Magnitude of strain rate dependency
E_0	Young's Modulus of the matrix material
ν_0	Poisson's Ratio of the matrix material
σ_0	Shear strength of the matrix material
h	Matrix properties
g	Matrix properties (Volumetric changes)
q	Void growth parameter
φ	Scaling Parameter for Pressure dependency
f_0	Density of voids

Table 2.3: Parameters Part B

C_R	Initial elastic modulus of Part B (stiffness in Langevin spring)
$\bar{\lambda}_L$	Locking stretch
κ	Bulk modulus (used in applications where only Part B is active)

2.3 Stress Triaxiality

The stress triaxiality is, besides the strain intensity, the most important factor that controls the initiation of a ductile fracture. When specimens are subjected to a tensile load a neck will form and induce significant modifications of the stress triaxiality ratio, which in turn will affect the stress - strain curves [Mirone, 2006]. The dominant failure mode for large triaxiality is void growth [Bao and Wierzbicki, 2004].

Commonly, the triaxiality σ^* is represented by the dimensionless stress triaxiality ratio, which is the relationship between hydrostatic stress σ_H and the equivalent von Mises stress σ_{eq} [Bridgman, 1964]

$$\sigma^* = \frac{\sigma_H}{\sigma_{eq}} = \frac{I_1/3}{\sqrt{3J_2}} \tag{2.30}$$

where

$$I_1 = \sigma_x + \sigma_y + \sigma_z \tag{2.31}$$

and

$$\sqrt{3J_2} = \sqrt{\sigma_x^2 + \sigma_y^2 + \sigma_z^2 - \sigma_x\sigma_y - \sigma_y\sigma_z - \sigma_z\sigma_x + 3(\tau_{xy}^2 + \tau_{yz}^2 + \tau_{zx}^2)} \tag{2.32}$$

thus Equation (2.30) can be written as

$$\sigma^* = \frac{(\sigma_x + \sigma_y + \sigma_z)/3}{\sqrt{\sigma_x^2 + \sigma_y^2 + \sigma_z^2 - \sigma_x\sigma_y - \sigma_y\sigma_z - \sigma_z\sigma_x + 3(\tau_{xy}^2 + \tau_{yz}^2 + \tau_{zx}^2)}} \tag{2.33}$$

Bridgman [1964] found that a relationship between σ_{eq} and σ_x, where σ_x is in the axial direction, could be expressed as

$$\frac{\sigma_x}{\sigma_{eq}} = 1 + \ln\left(\frac{a^2 + 2aR - r^2}{2aR}\right) \tag{2.34}$$

Here, a is the specimens radius in the necked zone, R the curvature radius of the neck and r the distance from the specimens centre axis. Assuming that the stress state in the notch is axially symmetric, that is $\sigma_y = \sigma_z$, Equation (2.30) can be written as

$$\sigma^* = \frac{\sigma_x}{\sigma_{eq}} - \frac{2}{3} \tag{2.35}$$

Then, Equation (2.34) becomes

$$\sigma^* = \frac{1}{3} + \ln\left(\frac{a^2 + 2aR - r^2}{2aR}\right) \tag{2.36}$$

The maximum value of σ^* is obtained in the centre of the specimen, where $r = 0$. Thus, combining Equations (2.35) and (2.36), the maximum value for σ^* will be

$$\sigma^*_{max} = \frac{1}{3} + \ln\left(1 + \frac{a}{2R}\right) \tag{2.37}$$

Further, the radial stress $\sigma_r = \sigma_y = \sigma_z$ can be found using the triaxiality ratio.

$$J_2 = \frac{1}{2}(\sigma'_{ij}\sigma'_{ji}) = \frac{1}{3}(\sigma_x^2 + \sigma_r^2 - 2\sigma_x^2\sigma_r^2) = \frac{1}{3}(\sigma_x - \sigma_r)^2 \tag{2.38}$$

The triaxiality factor can then be expressed as

$$\sigma^* = \frac{1}{3}\frac{\sigma_x + 2\sigma_r}{\sigma_x - \sigma_r} \tag{2.39}$$

solving for σ_r renders

$$\sigma_r = \sigma_x \cdot \frac{3\sigma^* - 1}{2 + 3\sigma^*} \tag{2.40}$$

When the notch radius is known, the stress triaxiality ratio in the centre of the notch can be calculated. This can be used to make a plot of the second

invariant as a function of the first from

$$\sqrt{3J_2} = \frac{I_1}{3\sigma^*_{max}} \tag{2.41}$$

and further to find the yield surface.

2.4 Prediction of Fracture

Damage can be described as the nucleation, growth and coalescence of microvoids or microcracks in solid materials. Looking at damage from a physical point of view, it is always related to plastic strains [Lemaitre and Desmorat, 2005].

When a specimen fractures - the elastic deformation will be reversed. Therefore, by measuring the area of the specimen immediately after fracture and comparing it to the initial area, the plastic strain at fracture p_f can be found [Clausen et al., 2003].

$$p_f = ln\left(\frac{L_f}{L_0}\right) \tag{2.42}$$

where L is the length of the specimen. Since polymer materials are used, the volume change has to be taken into account. The change can be described by

$$A_0 L_0 \exp(\epsilon_{vf}) = A_f L_f \tag{2.43}$$

thus

$$p_f = ln\left(\frac{A_0 \exp(\epsilon_{vf})}{A_f}\right) = ln\left(\frac{D_0^2 \exp(\epsilon_{vf})}{D_{f\perp} D_{f\parallel}}\right) = ln\left(\frac{D_0^2}{D_{f\perp} D_{f\parallel}}\right) + \epsilon_{vf} \tag{2.44}$$

D_0 represents the initial diameter of a specimen, measured before performing a test. $D_{f\perp}$ and $D_{f\parallel}$ represents the diameter of the specimen measured in two perpendicular directions immediately after the test. ϵ_{vf} is the true volume strain.

2.5 Fracture Surfaces

Compared to metals, fracture in polymers is in general more ductile. Even for fractures occurring at low temperatures, ductile deformed films and fibrils are visible at high magnifications. But, from a macroscopic point of view a brittle fracture for polymers still can be defined. Engel et al. [1981] defines a brittle fracture as a fracture producing fibrils less than $1\mu m$ long.

McCrum et al. [1997] states that whether a polymer, in any given circumstance, is ductile or brittle, depends upon it's resistance to yield and to crazing followed by crack propagation. Which of the two competing mechanisms who becomes the dominating one depends on temperature, strain rate, type of loading, component geometry and the presence of aggressive liquids. Normally, polymers such as HDPE and PVC will withstand a high degree of plastic deformation and behave as ductile materials [Engel et al., 1981].

Earlier at SIMLab, micrographs of the original microstructure of HDPE and PVC have been obtained by cooling down undeformed specimens in liquid nitrogen and breaking them, see Figure 2.5 and 2.6. The particles visible in the PVC material is calcium carbonate.

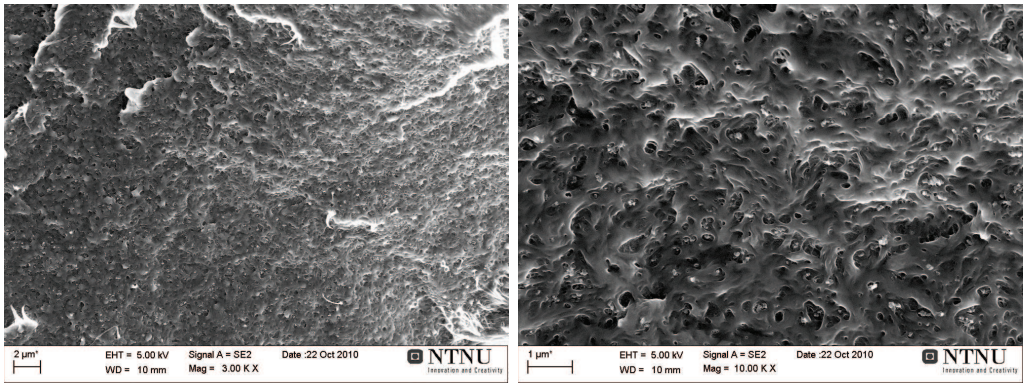

Figure 2.5: Fracture Surface of Undeformed HDPE

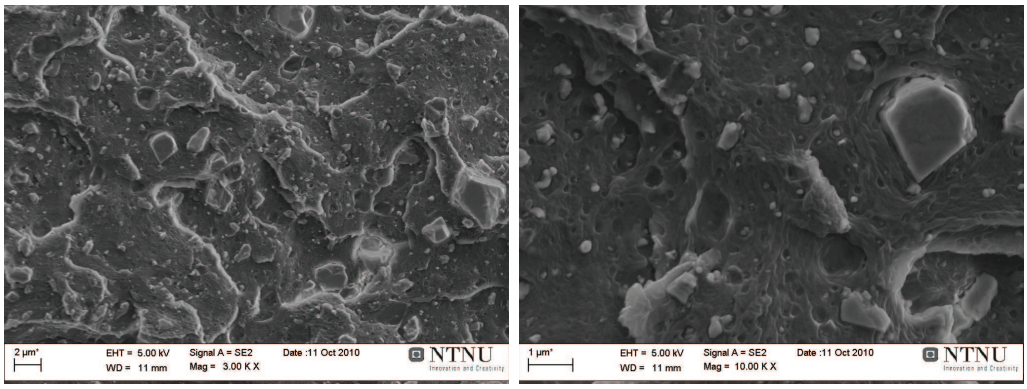

Figure 2.6: Fracture Surface of Undeformed PVC

By examining the fracture surfaces of tensile specimens of rubber-modified polypropylene reinforced by mineral particles Delhaye et al. [2010] observed two distinct morphologies. The initiation area, where the fracture initiated, is more ductile and consists of rather long pulling ligaments. The propagation area, where the crack rapidly propagated in the end of the fracture process, has more of a cleavage morphology. Examples are shown in Figure 2.7.

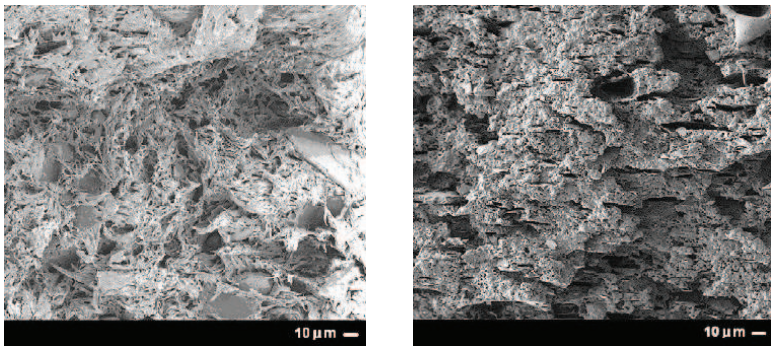

(a) Initiation area (b) Propagation area

Figure 2.7: Fracture Surface Morphologies [Delhaye et al., 2010]

Voids can occur when particles present in the material debonds from the matrix around them, or when the particle itself cavitates. On a larger scale,

cavitation can visually be observed as whitening of the material. It occurs when the stress level is close to the yield stress [Morawiec et al., 2001].

3

Materials and Laboratory Experiments

For investigation of how the plastic dilation in polymers is related to the triaxiality in stress, tensile tests of axisymmetric smooth and notched specimens were performed. The notched specimens had different notch radii, in order to obtain different triaxial stress states. This chapter first describes the materials used. The test method is then presented, followed by the post-processing of the tests and some basic test results. The main test results are presented, and compared to numerical simulations, in Chapter 5, and in Chapter 7 the results concerning fracture and fracture surfaces are presented.

3.1 Materials

Two different polymer materials were used, HDPE and PVC. They were made at SIMONA AG around three years before the testing took place. The materials were machined at NTNU into axisymmetric smooth and notched specimens.

3.1.1 HDPE

HDPE is a type of polyethylene (PE), which is an addition product consisting of the monomer ethylene shown in Figure 3.1. It has a high crystallinity,

about 75%. HDPE is a thermoplastic, and it is commonly used for producing tubes, bottles and household articles [Rösler et al., 2007].

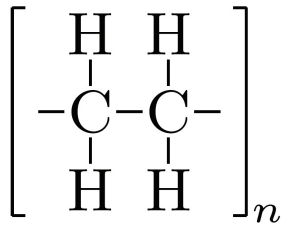

Figure 3.1: PE Monomer [Rösler et al., 2007]

From experimental testing to calibrate the material model employing the Raghava yield surface and plastic potential, and information from the material supplier SIMONA-AG [1995], Hovden [2010] found the HDPE used here to have the properties presented in Table 3.1.

Table 3.1: Mechanical Properties of HDPE

Part A		**Part B**	
$E\,[MPa]$	800	$C_R\,[MPa]$	1.74
ν_0	0.40	$\bar{\lambda}_L$	7.75
$\sigma_T\,[MPa]$	13.00	κ	0
α	1.00		
$\sigma_s\,[MPa]$	23.90	**Other**	
H	39.60	$K\,[MPa]$	1333
β	1.04	$G\,[MPa]$	286
$\dot{\epsilon}_0[s^{-1}]$	0.0007	$\rho\,[kg/m^3]$	950
C	0.108		

3.1.2 PVC

PVC consists of a monomer similar to ethylene, but with one hydrogen atom substituted by chlorine, see Figure 3.2. The chlorine atom changes

the performance of PVC compared to HDPE. T_g increases to 85 °C, and makes PVC relatively rigid at room temperature. PVC is a thermoplastic with a so low degree of crystallinity, about 5%, it is basically amorphous [Ram, 1997]. The low crystallinity is due to the fact that the chlorine atom takes up more space than a hydrogen atom, and makes it almost impossible for PVC to have crystalline regions. In addition PVC is usually modified by adding particles, which also makes it difficult to have crystalline regions.

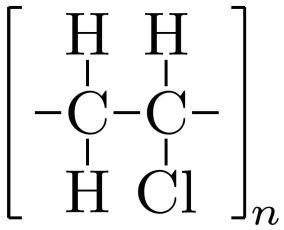

Figure 3.2: PVC Monomer [Rösler et al., 2007]

PVC can be combined with stabilisers, lubricants, plasticisers, fillers, pigments and other additives. This results in many different physical properties, depending on the additives. PVC has therefore many areas of application, including the production of tubes, packages, floor coverings and window frames [Ram, 1997].

When comparing PVC and PE, it is found that PVC is more stable towards the environment, more permeable and easier to modify using additives [Ram, 1997].

The mechanical properties for the PVC used here found from experimental testing to calibrate the material model employing the Raghava yield surface and plastic potential, and information from the material supplier SIMONA-AG [1996], by Hovden [2010] is presented in Table 3.2.

Table 3.2: Mechanical Properties of PVC

Part A		**Part B**	
$E\,[MPa]$	3000	$C_R\,[MPa]$	6.07
ν_0	0.30	$\bar{\lambda}_L$	1.71
$\sigma_T\,[MPa]$	46.80	κ	0
α	1.30		
$\sigma_s\,[MPa]$	37.80	**Other**	
H	15.00	$K\,[MPa]$	2500
β	1.27	$G\,[MPa]$	2142
$\dot{\epsilon}_0[s^{-1}]$	0.001	$\rho\,[kg/m^3]$	1430
C	0.070		

3.2 Test Method

In Figure 3.3 the geometry of the specimens made for the tests are shown. The geometry of the smooth specimens is shown to the left, and the geometry of the other specimens to the right.

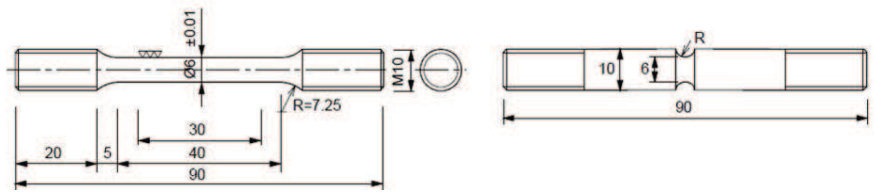

Figure 3.3: Geometry of Specimens $[mm]$

The notched specimens had four different initial notch radii: $R = 0.8mm$, $R = 2mm$, $R = 5mm$ and $R = 20mm$. All the different geometries were represented in each material, adding it up to ten different tests in total. They were named on the form (material)_R(radius)_(test no.), e.g. for the

first test of a PVC specimen with $R = 2mm$, the name would be PVC_R2_1. The smooth specimens were named as (material)_smooth_(test no.).

To map displacements and other geometry changes during the tests, a custom made DIC algorithm was created. The tests were monitored by a CCD camera creating pictures for input to the DIC code. Markings were applied to the surface of the notch of the specimens prior to the tests, to be able to map the deformations.

A line of small dots were applied as markings as reference points for the DIC, starting $1mm$ from the centre of the specimen to each side, continuing with $1mm$ distance to the edge of the curved surface of the specimen, see Figure 3.4(a). The light grey PVC was marked with black dots, and the black HDPE with white dots. A microscope was used to obtain the desired accuracy of the placing of the dots, see Figure 3.4(b).

(a) Marked Specimens

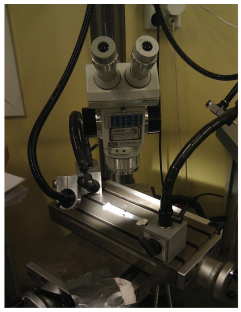

(b) Microscope used for Marking

Figure 3.4: Preparation of Specimens

Earlier at SIMLab, another DIC technique, similar to the one described by Hovden [2010] and Kamaya and Kawakuboa [2011], had been applied to the same test set; introducing small black dots on the surface of the specimens and mapping the deformation of the specimens using the DIC software 7D to compare images acquired with a CCD camera during the tests. The test set had been carried out twice, with two different grades of fine-grained patterns. None of the test sets were however successful in representing the stress and

strain fields for the specimens correctly, because of the large displacements over relatively small areas. Also, the old method was not able to both map the strain field of the front of the specimen and measure the changes in the specimens contour at a time; focusing on one of them during a test would make the other one diffuse and impossible to measure.

A new approach, using a custom made DIC algorithm, was therefore employed. The custom made script returns the desired measures for all the pictures taken during a test. From these measures deformations, stresses and strains could be calculated. During the tests, only one camera was used, and thus only planar displacements and strain fields could be mapped.

Several tests were performed for each different specimen to prove the repeatability. The tests were performed using a Dartec M 1000 RK machine with a 20 kN load cell, see Figure 3.5(a), connected to an Instron controller, see Figure 3.5(b). The Instron controller logged time, displacement and force with the same frequency as the pictures were taken, with the software Wave Matrix. To monitor the deformation of the specimens, a Prosilica GC2450 CCD camera was placed on a tripod facing the dotted side of the specimens, taking one picture per second. For PVC_R08 and PVC_R2 pictures were taken twice per second. The pictures were taken using the software SAVEN-GV.

To make the post-processing of the tests easier, a black plate for the light grey PVC and a white plate for the black HDPE were placed behind the testing machine, so a sharp contrast between the specimens and the background was obtained. Three light units were also used, directed towards what would be the edges of the specimens in the pictures, to make the contour as sharp as possible.

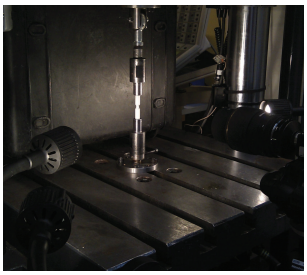

(a) Dartec Machine

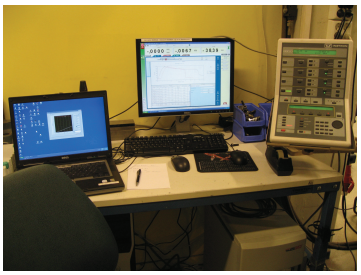

(b) Instron Controller

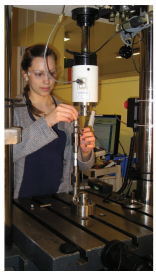

(c) Mounting

Figure 3.5: Laboratory Testing

The same global strain rate $\dot{\epsilon}$ and cross head deformation speed v was used for all samples

$$\dot{\epsilon} = 10^{-3}\, s^{-1} \tag{3.1}$$

$$v = 0.04\, mm/s \tag{3.2}$$

Thus, the tests could be characterised as quasi-static. At a strain rate this low, temperature effects, which are not included in the material model, are assumed to be negligible.

3.3 Post-processing

3.3.1 Extraction of Force - Displacement Curves

Initial noise may occur in force-displacement curves extracted from tension tests due to the fact that the specimens may not be totally fixed in the test machine. Thus crosshead displacement may be registered even though there is none. This initial noise may be removed from the curves by using a method from Lemaitre and Chaboche [1990], see Figure 3.6.

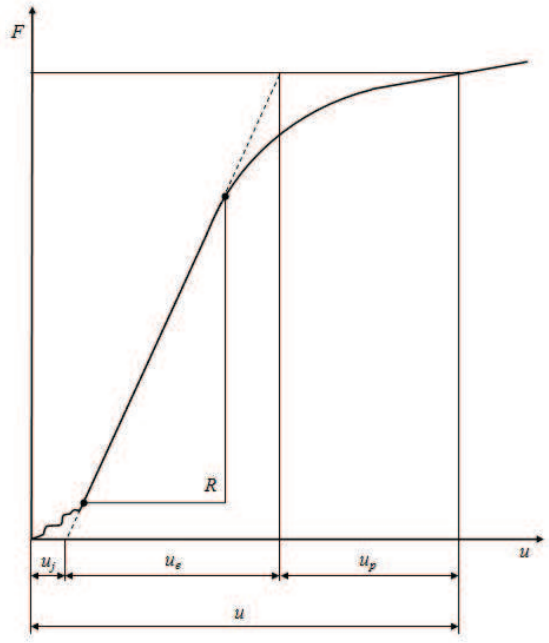

Figure 3.6: Force - Displacement Curve [Lemaitre and Chaboche, 1990]

First, the stiffness is derived from the data from the elastic area, thus over the displacement u_e. This is done by using a curve fitting tool in e.g. the numerical computing environment and programming language MATLAB, finding a linear polynomial fitting the line, resulting in an equation on the form

$$F = au + b \tag{3.3}$$

Then, since the deformation so far is elastic, the stiffness is used to find the initial displacement u_j.

$$u_j = \frac{-b}{a} \tag{3.4}$$

The force - displacement curve is then shifted sideways a distance u_j and the straight line in the elastic area is extended to the origin.

3.3.2 Yield Stress

There are different methods that can be used to determine the yield stress. If the true stress - true strain curve shows a clear first maximum, this maximum value can be used for the yield stress, as used in the calibration of the material model for PVC by Hovden [2010]. This equals the point where the tangent to the true stress - true strain curve is horizontal, $d\sigma/d\epsilon = 0$ (see Figure 3.7).

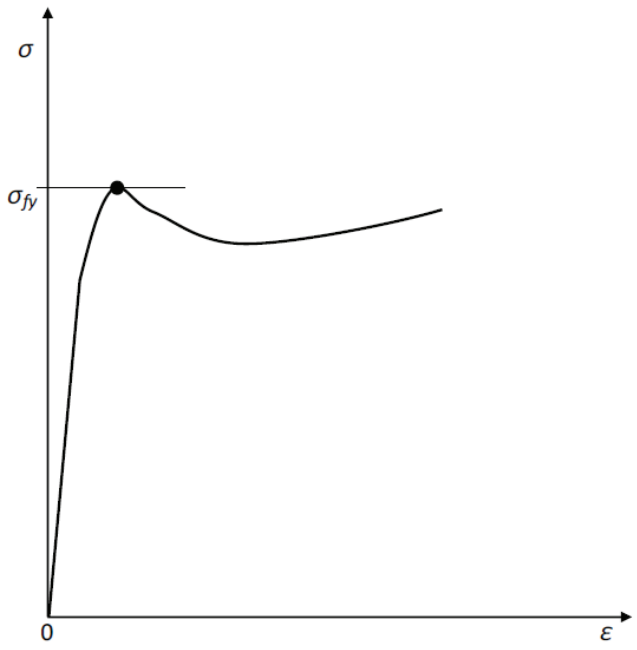

Figure 3.7: Using $d\sigma/d\epsilon = 0$ to Determine the Yield Stress

If such a maximum point is difficult to find, Considère's construction can be applied. Considère's construction assumes that the material is rate-insensitive. The extension ratio is defined as [McCrum et al., 1997]

$$\lambda = \frac{L}{L_0} \tag{3.5}$$

The volume is not constant during the deformation. However, when using Considère's construction for ductile polymers, such as HDPE and PVC, the

volume can be approximated to a constant one [McCrum et al., 1997]. Thus

$$A_0 L_0 = AL \tag{3.6}$$

$$A_0 = A\lambda \tag{3.7}$$

Using the true stress σ_t and the engineering stress σ

$$F = \sigma_t A = \sigma A_0 \tag{3.8}$$

thus

$$\sigma = \frac{\sigma_t}{\lambda} \tag{3.9}$$

If σ and λ is plotted against each other the slope of this plot will be

$$\frac{d\sigma}{d\lambda} = \frac{1}{\lambda}\frac{d\sigma_t}{d\lambda} - \frac{\sigma_t}{\lambda^2} \tag{3.10}$$

At yield both $d\sigma/d\epsilon = 0$ and $d\sigma/d\lambda = 0$, thus

$$\frac{d\sigma_t}{d\lambda} = \frac{\sigma_t}{\lambda} \tag{3.11}$$

According to this equation, in a plot of σ_t versus λ yield will occur where a tangent can be drawn from the origin to the nominal stress - extension ratio curve at a point M, as shown in Figure 3.8.

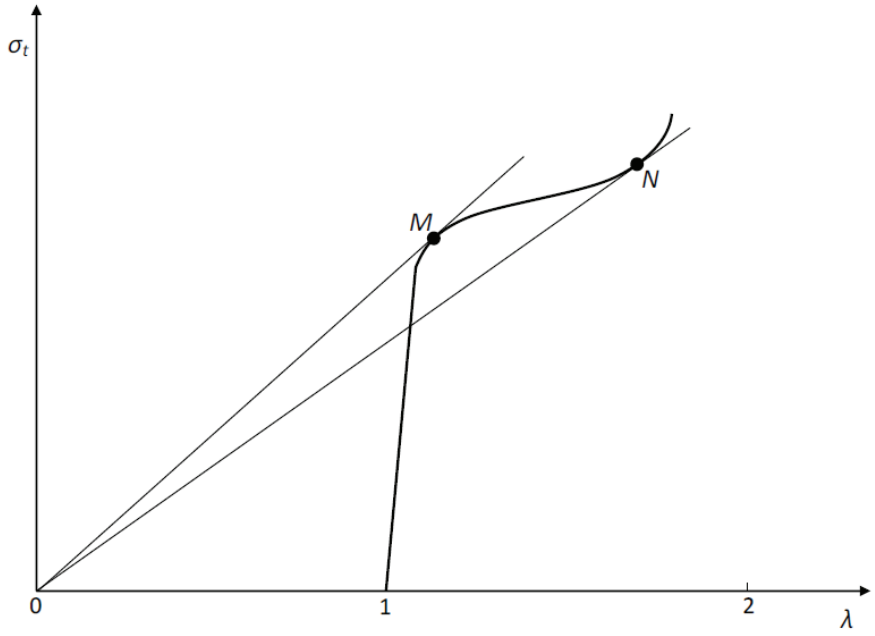

Figure 3.8: Considère's Construction [McCrum et al., 1997]

3.3.3 Necking and Cold-Drawing

In Figure 3.8 it is also shown how it, in some cases, is possible to find a second tangent from the origin crossing the curve at a point N. This point defines a minimum in the true stress - extension ratio curve, and here the molecular orientation stiffens the drawn polymer in the neck to resist further extension. After point N the neck stabilises and extends by drawing fresh material from either side of the neck [McCrum et al., 1997]. This is defined as cold-drawing. The conditions for cold-drawing are satisfied if both a point M and N can be found [Vincent, 1959].

Cold-Drawing takes place because of a mechanical instability. This instability is caused by the increase in a polymers modulus when subjected to tensile forces, and it makes the stress-strain curve bend downwards. Necking will then initiate as a consequence of the instability and further the molecules will be oriented, and cause a strain-hardening process where cold-drawing occurs.

Insufficient strain-hardening will hinder cold-drawing [Vincent, 1959].

3.3.4 Interpreting Images

To extract desirable data from the tests, a custom made DIC algorithm was created. The algorithm was implemented in MATLAB. It was desirable to map the smallest diameter D, the radius of the neck in the centre of the contour R and the volume V between the dots nearest to the centre of the specimen, and the distance L between these dots, for each picture (see Figure 3.9). In the following a description of the script is presented. A representative example of the algorithm as used in the post-processing is included in Appendix A.

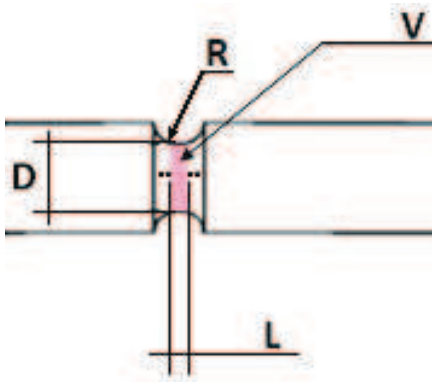

Figure 3.9: Sizes Returned from MATLAB Script

The MATLAB script uses all pictures taken during a given test as input, and maps displacements by comparing the pictures. First, two methods are called for each picture in turn. The first method, illustrated in Figure 3.10, makes the picture black and white, and finds the edge of the specimen (see step 1 in Figure 3.10) and the smallest diameter D (see step 2 in Figure 3.10).

Further the middle of the specimen is located, and the distances from the middle out to the two nearest dots is found and added together to give the distance between them, L (see step 3 in Figure 3.10). Then, the method finds the volume of the specimen between the dots by calculating the volume

of small discs, enclosed by the edge that was found, from the centre and out to the nearest dots. Each disc has the height of one pixel, and adding the discs up gives the total volume V (see step 4 in Figure 3.10).

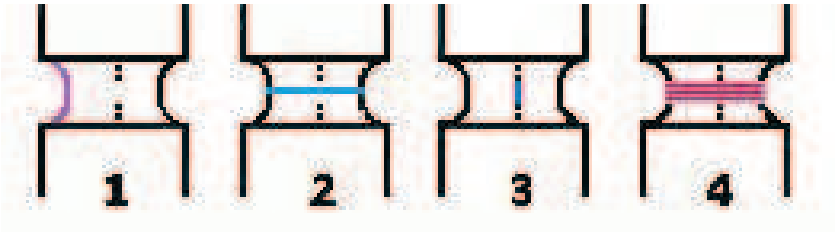

Figure 3.10: Illustration of Steps in First Method

The second method, illustrated in Figure 3.11, uses the contour of the specimen and finds the circle that best fits the neck in the centre of the contour. The best fitting circle is found using the method of least squares on the distance between the contour and the circle (turquoise area in step 1 in Figure 3.11) to minimise the distance. This is done by using the built-in MATLAB function lsqnonlin, which solves nonlinear least-squares problems. The circle is then used to calculate the radius of the root of the notch, R. As a visual control, small stars are plotted where the diameter search starts and ends, and where the search for the dots starts and ends. The best fitting circle is also plotted, see Figures 3.12 and 3.13.

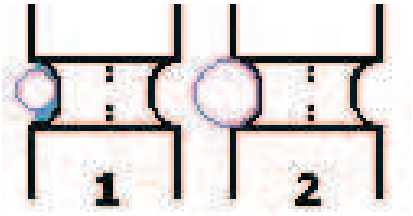

Figure 3.11: Illustration of Steps in Second Method

Last, the script converts D, L, V and R from pixels to millimetres. The relationship between pixels and millimetres is found using the image processing program ImageJ, counting the number of pixels for certain distances

in images of the specimens, and comparing them to measurements of the same distances done directly on the specimens.

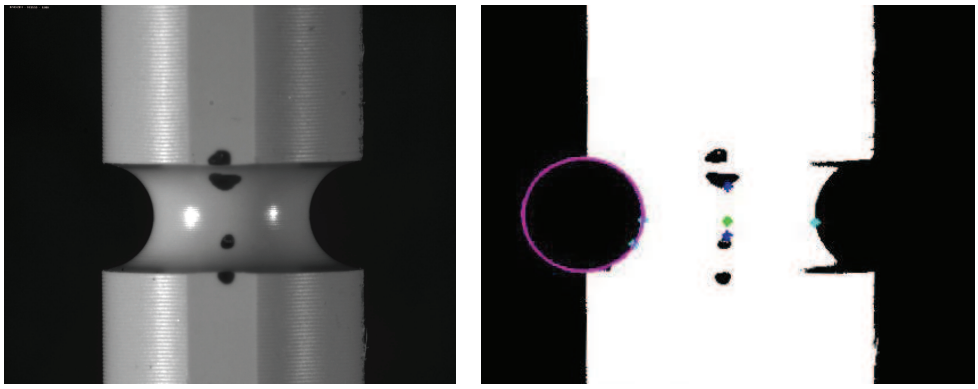

(a) Picture from Test (b) Picture in MATLAB

Figure 3.12: Post-processing in MATLAB of PVC_R2

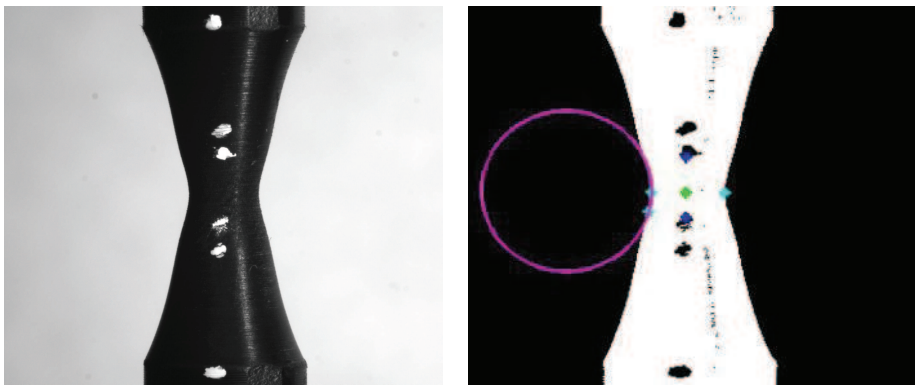

(a) Picture from Test (b) Picture in MATLAB

Figure 3.13: Post-processing in MATLAB of HDPE_R20

To ensure that the MATLAB script gave correct results, hand measurements of a selection of pictures from every test was performed for comparison, using ImageJ.

All the sizes found in MATLAB were plotted against the crosshead displacement, to easier discover errors or irregularities. Further, plots such as true stress - true strain and true volume strain - true strain were made.

3.3.5 Calculation of Stresses and Strains

Using the measures shown in Figure 3.9, stresses and strain could be calculated. From the distance L, the longitudinal true strain could be calculated as

$$\epsilon_l = \ln\left(\frac{L}{L_0}\right) \tag{3.12}$$

assuming homogeneous strain over L, where L_0 is the initial length of the distance. The radial true strain could be calculated in the same manner using the smallest diameter D

$$\epsilon_r = \ln\left(\frac{D}{D_0}\right) \tag{3.13}$$

where D_0 is the initial diameter of the specimen. Further, the smallest diameter D could also be used to find the smallest area at all times, and thus the largest longitudinal true stress

$$\sigma_l = \frac{F}{(\pi D^2/4)} \tag{3.14}$$

The true volume strain could be found using

$$\epsilon_V = \ln\left(\frac{V}{V_0}\right) \tag{3.15}$$

assuming homogeneous volume strain over V, where V_0 is the initial volume of the region.

3.4 Basic Test Results

To ensure that each experimental test was correct and accurate, a test was performed several times to prove its repeatability.

3.4.1 Key Values

Summaries of key values from the third test set are shown in Tables 3.3 and 3.4. Δ_{max} is the maximum crosshead displacement each test was elongated to, while F_{max} is the maximum registered force. σ_T is the yield stress that was found for each specimen.

Table 3.3: Summary of Results from HDPE Tests

Test	$\Delta_{max}[mm]$	$F_{max}[N]$	$\sigma_T[MPa]$
HDPE_R08_3	4.0	949	38.1
HDPE_R2_3	7.1	889	34.5
HDPE_R5_3	9.3[1]	832	32.3
HDPE_R20_3	9.4[1]	694	27.7
HDPE_smooth_3	26.0[1]	592	21.5

Table 3.4: Summary of Results from PVC Tests

Test	$\Delta_{max}[mm]$	$F_{max}[N]$	$\sigma_T[MPa]$
PVC_R08_3	1.9	1563	55.2
PVC_R2_3	2.1	1549	55.0
PVC_R5_3	3.4	1543	55.9
PVC_R20_3	6.2	1472	52.2
PVC_smooth_3	9.03	1304	47.7

[1]The test was stopped before the specimen ruptured

3.4.2 Force - Displacement Curves

In Figures 3.14 and 3.15, the force - displacement curves for HDPE_R20 and PVC_R20 are shown. All of the force - displacement curves are shown in Appendix B.

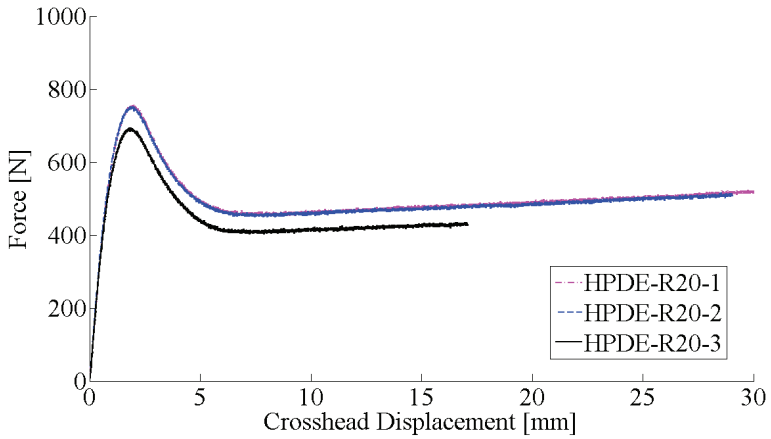

Figure 3.14: Force - Crosshead Displacement for HDPE_R20

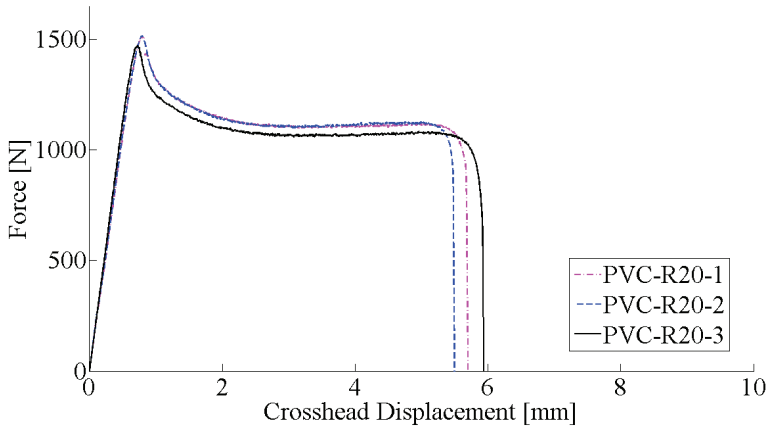

Figure 3.15: Force - Crosshead Displacement for PVC_R20

3.4.3 Yield Stress

The yield stress for the PVC specimens was found using the first maximum stress value on the true stress - true strain curve. For the HDPE specimens however, such a maximum point was hard to define for the largest notch radii. Therefore, Considère's construction was applied to all the HDPE specimens.

Both of the methods for determining the yield stress are described in Section 3.3.2. The methods are consistent with the ones used in the calibration of the material model employing the Raghava yield surface and plastic potential for HDPE and PVC by Hovden [2010].

The yield points of all curves are in the following plots marked with a black circle.

3.4.4 Necking and Cold-Drawing

All the PVC specimens fractured before cold-drawing occurred. For all the HDPE specimens however, cold-drawing could be observed. For the HDPE specimen with the highest triaxiality, HDPE_R08, the onset of cold-drawing coincided with the yield point.

In the following plots, the points where cold-drawing started are marked with a magenta coloured circle for all curves.

The point at which cold-drawing started can be seen in a radius - crosshead displacement plot, see Figure 3.16, where the radius is calculated from a circle placed in the root of the notch.

The moment when the local radius starts to decrease is defined as the onset of necking. Cold drawing starts when the neck propagates, observed as an increase of the radius value.

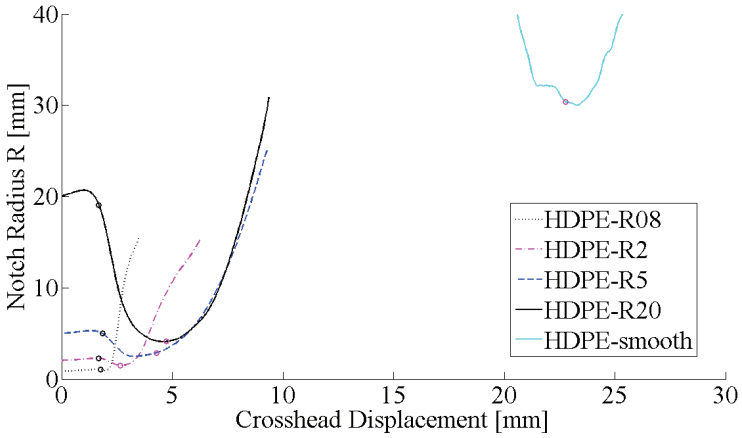

Figure 3.16: Radius versus Crosshead Displacement for HDPE

3.4.5 Evaluation of Basic Test Results

From Figures 3.14 and 3.15 it can be seen that the repeatability of the tests is very good. The other force - displacement curves, shown in Appendix B, were even closer together than the ones shown in Figures 3.14 and 3.15.

4

Numerical Simulations

The numerical simulations are performed for two purposes: To validate the method used in the post-processing of the tests and to reveal possible deviations between the material model used for the simulations and the material behaviour in the tests.

In this chapter the modelling and the simulations are described, together with some basic simulation results. Further, in Chapter 5, the main simulation results are presented and compared to the test results.

4.1 Modelling

The specimens were modelled using the finite element software LS-DYNA. A representative keyword-file for the modelled specimens can be found in Appendix C. One of the modelled specimens is shown in Figure 4.1.

The cross-section of the same specimen is shown in Figure 4.2, and it shows how the elements are partitioned to avoid triangular elements in the centre. Key data for the specimens is given in Table 4.1.

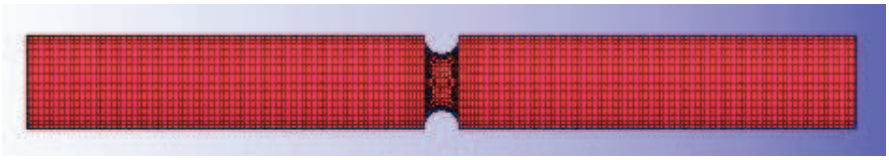

Figure 4.1: R2 Modelled in LS-DYNA

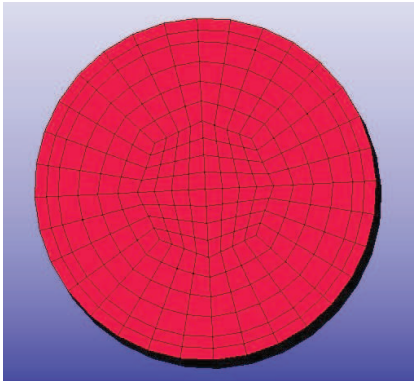

Figure 4.2: Cross-Section of LS-DYNA Model

Table 4.1: Key Data for Specimens

Specimen	**Element type**	**Nodes**	**Elements**
R08	Solid	64559	57000
R2	Solid	50443	43136
R5	Solid	51375	44032
R20	Solid	51375	44032
Smooth	Solid	41256	36000

For the modelling of the specimens the element formulation used was EQ1 - Constant stress solid elements. This means that the elements behave essentially as nonlinear, to be able to permit the severe distortions sometimes seen in honeycomb materials [LSTC, 2007]. The elements are shorter in the longitudinal direction than in the two other directions. This was done to improve aspect ratios as strains grow large in the necking zone. The notch of

the specimens were modelled with smaller elements since the deformations were larger here.

The specimens were fixed in all directions at one end, and a displacement was applied in the longitudinal direction at the other end, using a smooth amplitude function. In the moving end, displacements in all directions except the longitudinal one were fixed. The material model used was the SIMLab developed model using the Raghava yield criterion and plastic potential. Tables 3.1 and 3.2 shows the material parameters used for the simulations for HDPE and PVC respectively.

All the information from the simulations were extracted in the same way as for the tests, to get a better basis for comparison with the tests.

In the modelling the set of consistent units *tonne*, *mm*, *s*, *N* and *MPa* was used.

4.2 Results

In Figures 4.3 and 4.4 the force - crosshead displacement curves for all the specimens simulated are shown.

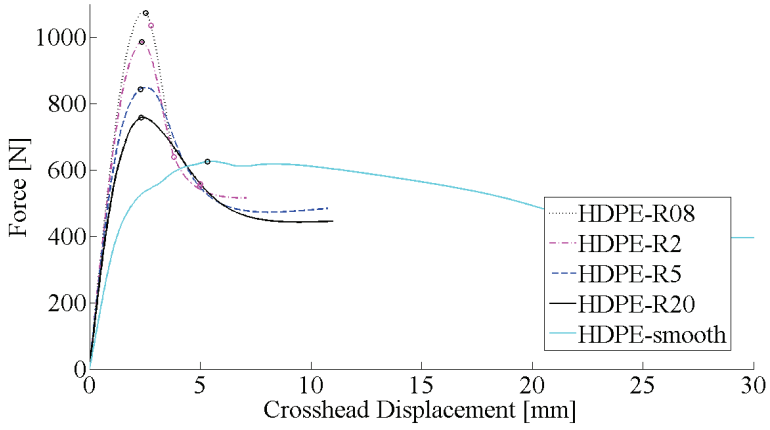

Figure 4.3: Force - Crosshead Displacement for HDPE Simulations

As can be seen the force - displacement curves from the simulations resemble the force - displacement curves from the tests, shown in Appendix B.

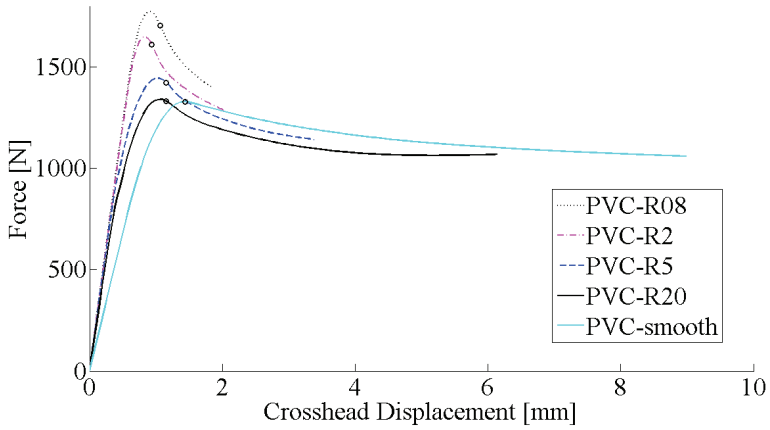

Figure 4.4: Force - Crosshead Displacement for PVC Simulations

4.3 Evaluation of Simulations

From Figure 4.4 it looks as though the different simulations of the specimens had different stiffness. An analysis with an, in comparison, infinite large yield stress was therefore carried out, to check if the stiffness in fact varied for the different specimens simulations. The result can be seen in Figure 4.5.

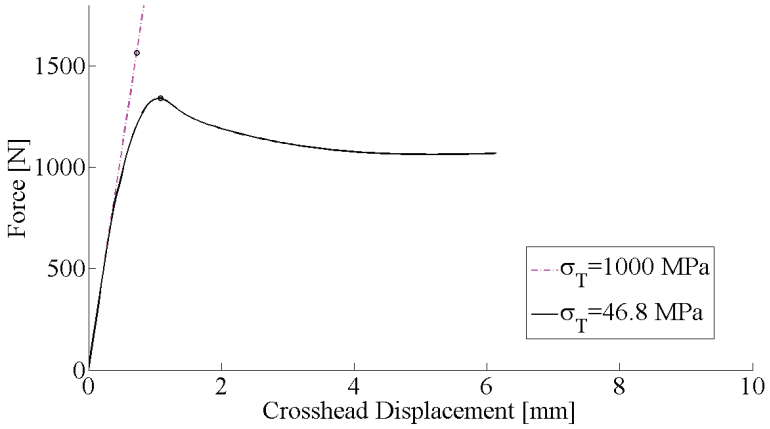

Figure 4.5: Simulations Using Different Yield Strength for PVC_R20

Clearly, the stiffness is the same for the different simulations. The apparent deviations in stiffness originates from the initiation of yielding in some elements, which makes the curves soften.

To reduce the central processing unit (CPU) time, mass scaling was introduced in the simulations. First, the mass was scaled with a factor 10^9, however this gave an unstable force, as shown for PVC_R2 in Figure 4.6. The effect decreased when less mass scaling was used.

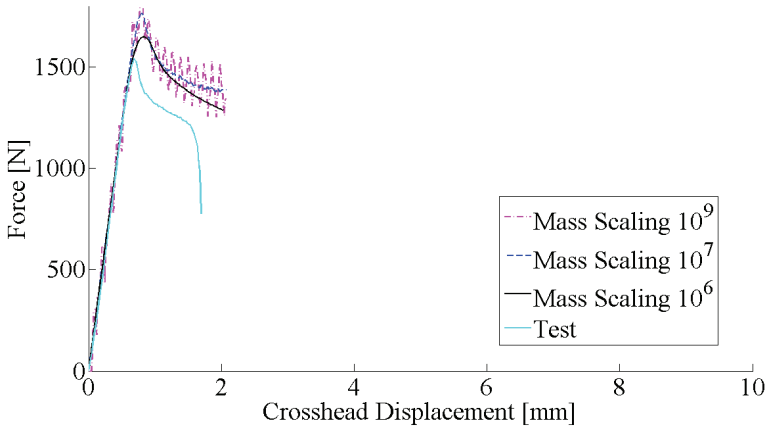

Figure 4.6: Comparison of Different Mass Scaling with Test Result

As can be seen, the force converges towards the test result the less the mass is scaled. It was however chosen to not scale the mass less than with a factor 10^6, since this would give a CPU time of 7 days or longer, depending on the specimen simulated.

The ramping of the force was also varied to see if it could make the load path smoother, and both a normal load curve definition and a smooth load curve definition was tested. However, none of the attempts had any notable effect on the smoothness of the curve.

To measure the radius in the simulations correctly, calculated from a circle placed in the root of the notch, was difficult because of the mid elements being largely stretched out. This in turn affected the triaxiality. It was also difficult to define an initial length and an initial volume that had the exact same size as the ones used in the tests, since the initial length and volume had to be defined using the existing element partitioning.

Energy Balance

In Figure 4.7 the total energy for the analysis of HDPE_R2 is compared with the external work.

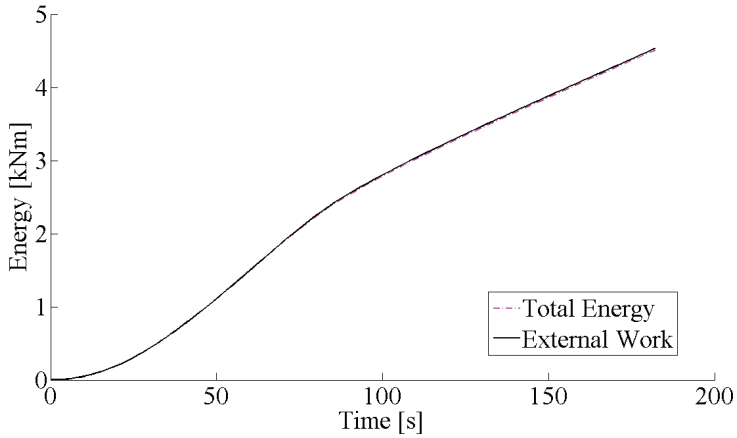

Figure 4.7: Comparison of the Total Energy and the External Work

It can be seen that the total energy is constant in comparison to the external work. A comparison of the values show that they never deviate with more than 0.5%.

The internal energy and the hourglass energy for the analysis of HDPE_R2 are compared in Figure 4.8.

As shown, the hourglass energy is relatively low compared to the internal energy. At most the hourglass energy is 5.2% of the internal energy.

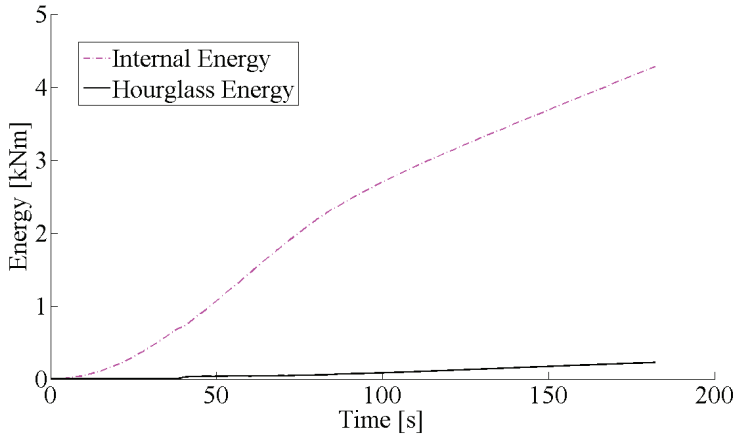

Figure 4.8: Comparison of the Internal Energy and the Hourglass Energy

In Figure 4.9 the kinetic energy is compared to the internal energy for the analysis of HDPE_R2.

As can be seen, the kinetic energy is negligible in comparison to the internal energy. A comparison shows that the value for the kinetic energy is at most approximately 0.01% of the value for the internal energy.

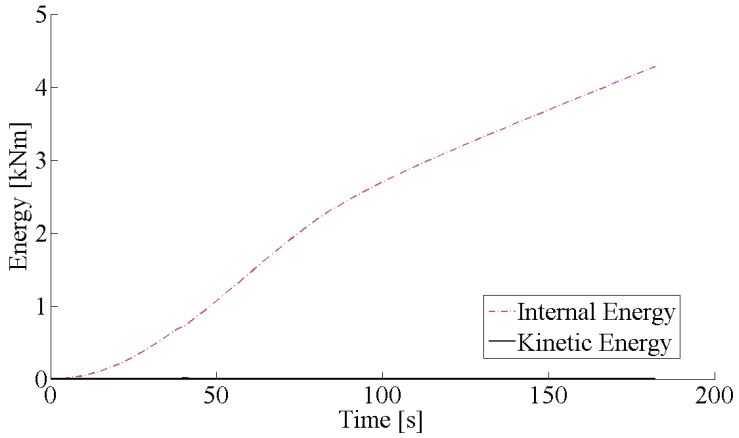

Figure 4.9: Comparison of the Internal Energy and the Kinetic Energy

For all simulations the energy comparisons described here has been checked. None of them deviated significantly from the comparisons shown above.

5

Tests and Simulation Results

To find possible deviations between the material model used for the simulations and the material behaviour in the tests, the results from both were compared. In this chapter the main results from the tests and simulations are presented and compared.

The smooth specimens in the tests fractured differently than expected. It seemed as if the fractures developed along a spiral pattern on the outside of the specimens. Since this happened to each and all of the smooth specimens it is assumed to be an effect from the machining. The results from the smooth specimens are therefore not included in all the plots.

5.1 Results

5.1.1 True Stress - True Strain

In Figures 5.1 and 5.2, the true longitudinal stress - true longitudinal strain curves for HDPE tests and simulations are compared. Figures 5.3 and 5.4 shows the same comparison for PVC.

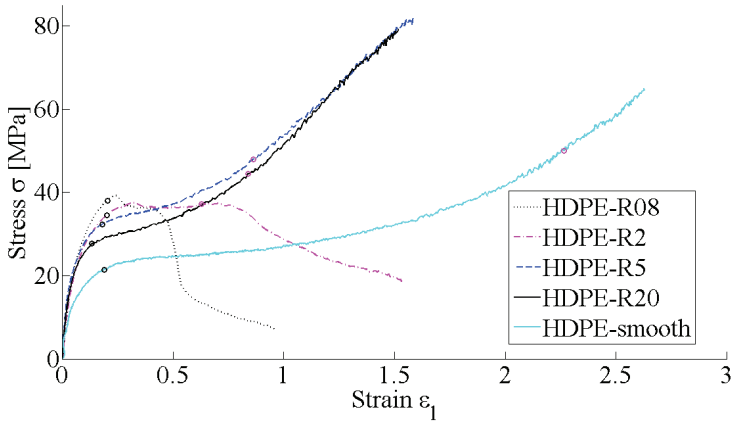

Figure 5.1: True Stress - True Strain Curves for HDPE Tests

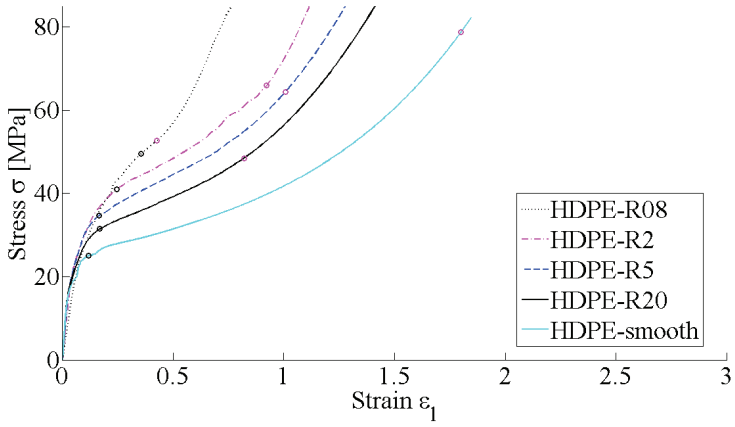

Figure 5.2: True Stress - True Strain Curves for HDPE Simulations

As can be seen the curves for both HDPE and PVC commence with a steep slope, this is related to the inter-molecular forces. The slope starts to gradually flatten right before the yield point, because yield is reached in some parts of the specimens before the yield point. An apparent trend is that the yield stress increases when the initial notch radius decreases, especially for HDPE.

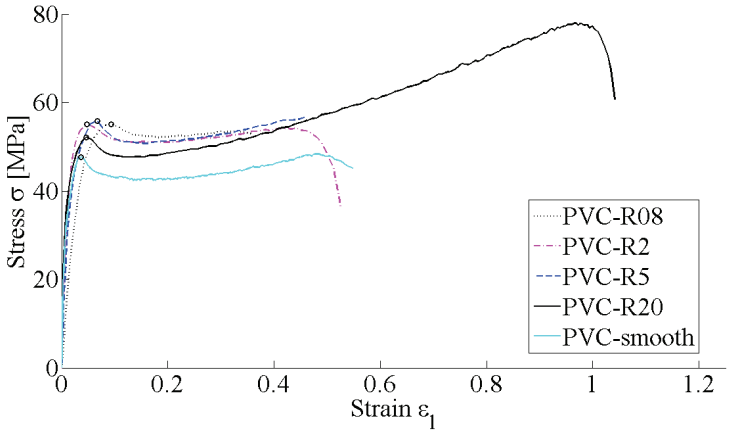

Figure 5.3: True Stress - True Strain Curves for PVC Tests

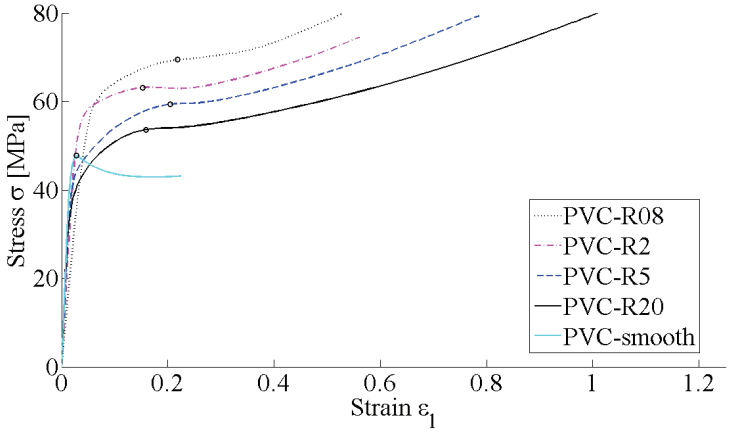

Figure 5.4: True Stress - True Strain Curves for PVC Simulations

During the deformation in the laboratory tests of these materials two mechanisms compete: The stretching of the molecular network increases the stiffness, while damage due to void growth tends to soften the material. After yield the curves for HDPE_R08 and HDPE_R2 bottoms out because of the damage triumphing the network forces, while the curves for the other three specimens surges due to the network forces dominating over the damage. For PVC all the test curves peaks when yield is reached.

Young's modulus was found to be in agreement with the values found by Hovden [2010] for both HDPE and PVC in uniaxial tension, see Tables 3.1 and 3.2. The yield stress and the start of cold-drawing for the simulations were found in the same manner as for the tests.

5.1.2 Local Strain Rate

In Figures 5.5 and 5.6 for HDPE and Figures 5.7 and 5.8 for PVC, true longitudinal strain is plotted against time.

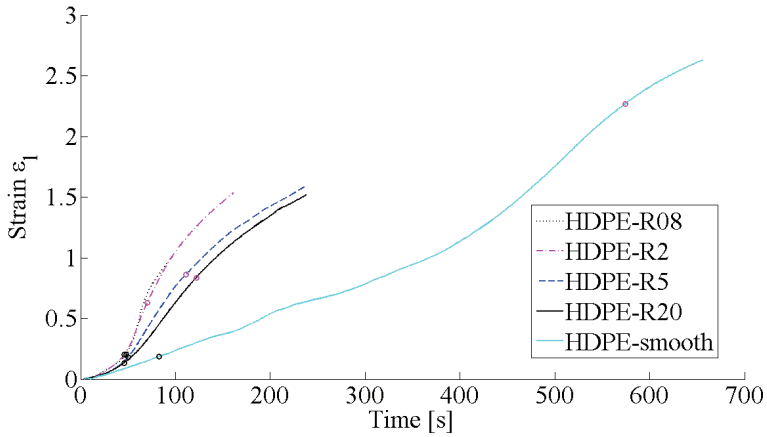

Figure 5.5: Local Strain Rates for HDPE Tests

The slope will thus represent the local strain rate for the area between the two dots closest to the centre used to measure the distance L (see Figure 3.9).

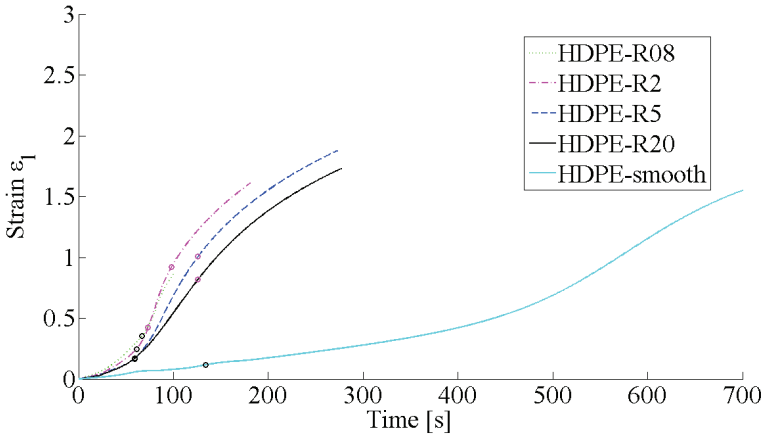

Figure 5.6: Local Strain Rates for HDPE Simulations

As can be seen, the local strain rate varies with initial notch radius, and as expected the local strain rate is higher for the specimens with the smallest notch radii.

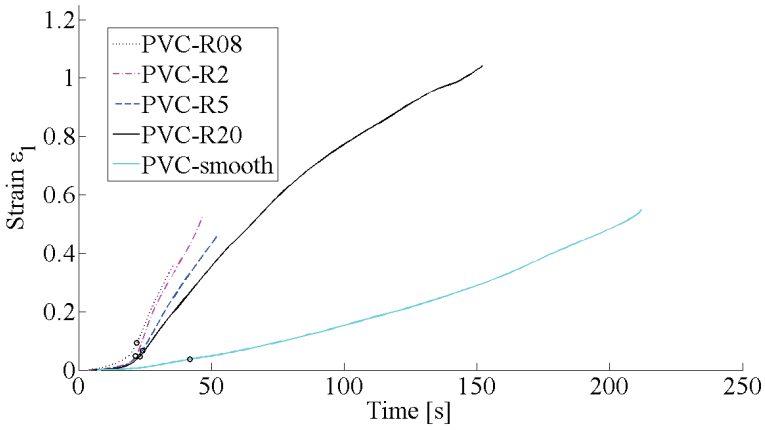

Figure 5.7: Local Strain Rates for PVC Tests

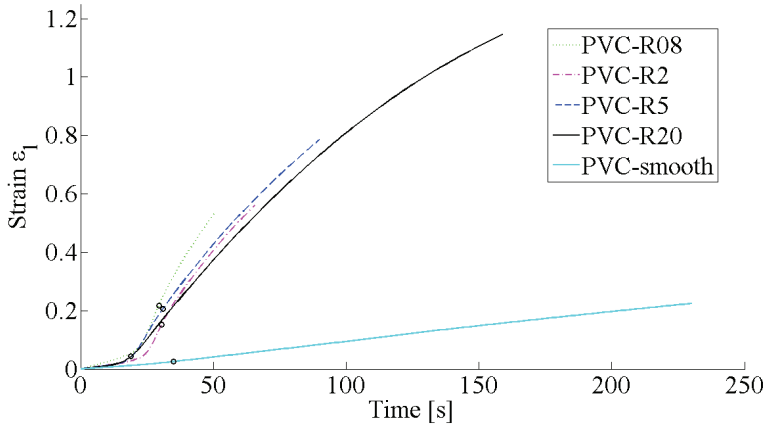

Figure 5.8: Local Strain Rates for PVC Simulations

5.1.3 Triaxiality

In Figures 5.9 and 5.10 a plot of the true longitudinal strain versus the stress triaxiality for PVC is shown. The calculation of the stress triaxiality is described in Section 2.3. A black x is used to mark the point of fracture. The current material model does not contain a fracture criterion, so a point of fracture cannot be found for the simulations. This is solved by assuming fracture after the same amount of elongation before fracture as for the tests.

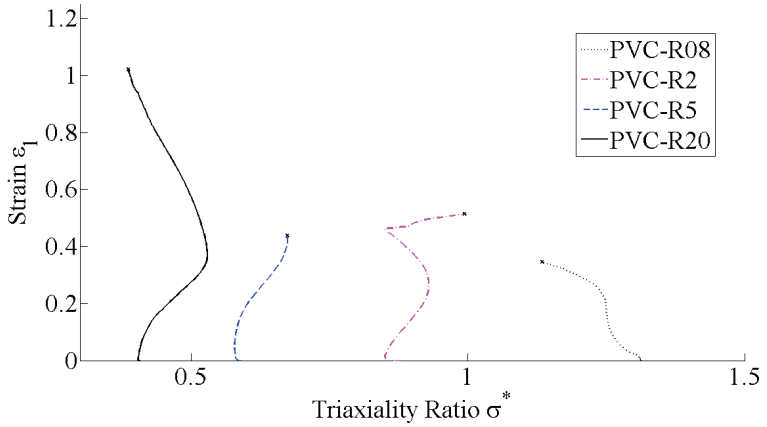

Figure 5.9: Stress Triaxiality for PVC Tests

The figures shows that the specimens have non-proportional load paths, though the paths are somewhat more uniform for the simulations.

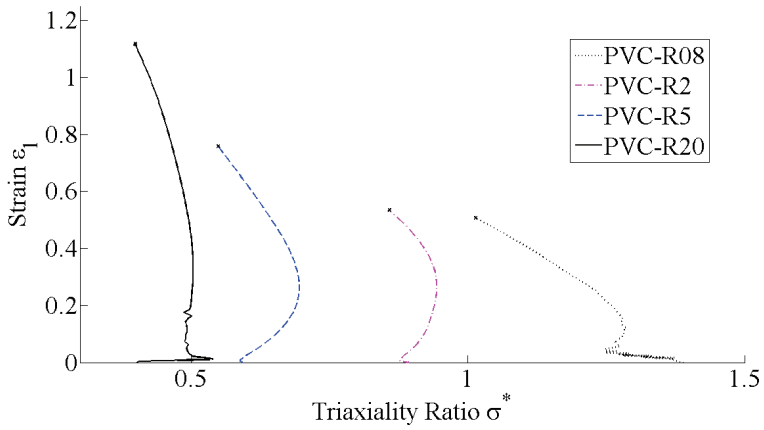

Figure 5.10: Stress Triaxiality for PVC Simulations

It can also be seen from the figures, although not entirely consistent, that a smaller initial notch radius leads to a higher longitudinal strain before fracture.

5.1.4 Yield Surface

In Figures 5.11 and 5.12 for HDPE and Figures 5.13 and 5.14 for PVC, the equivalent von Mises stress plotted against the hydrostatic stress. Also, the yield surfaces for a strain rate equal to zero, defined by the parameters in the material model is shown in each plot.

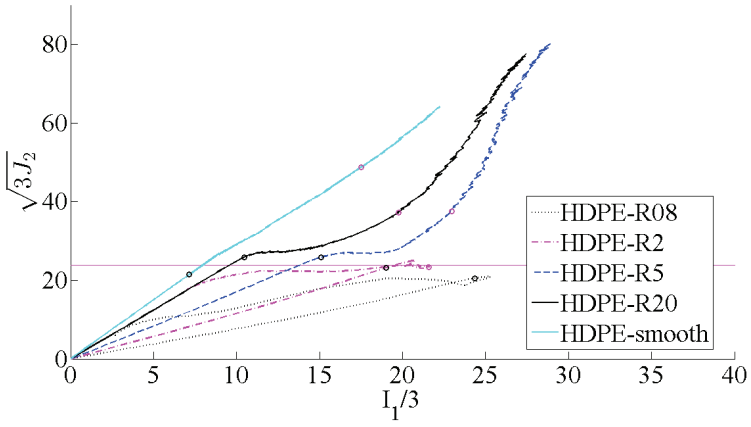

Figure 5.11: Yield Surface for HDPE Tests

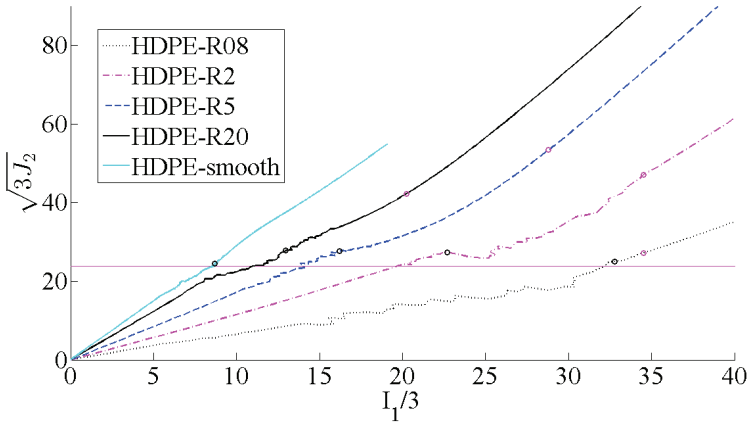

Figure 5.12: Yield Surface for HDPE Simulations

The hydrostatic stress is calculated using Equation (2.40) to find the radial stress with $\sigma_r = \sigma_y = \sigma_z$, and the yield surface is found using the Raghava yield criterion. As can be seen, some of the curves has a sudden shift in directions. This is due to the fact that the Bridgman equation only is valid up to a certain point of the curves. It can also be seen that the yield points from the simulations tends to lie a bit above the yield surfaces.

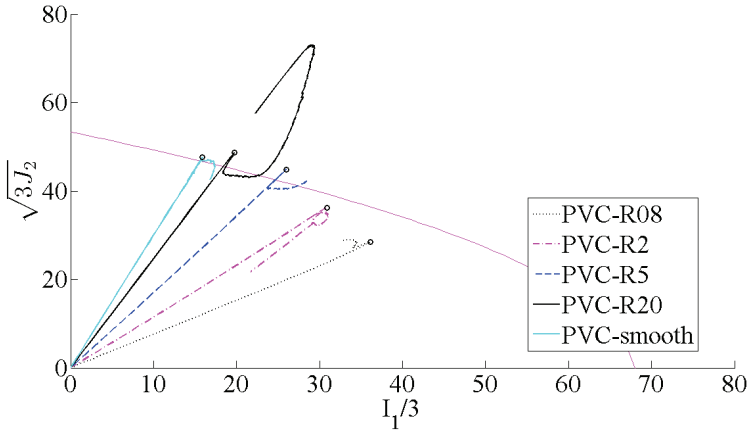

Figure 5.13: Yield Surface for PVC Tests

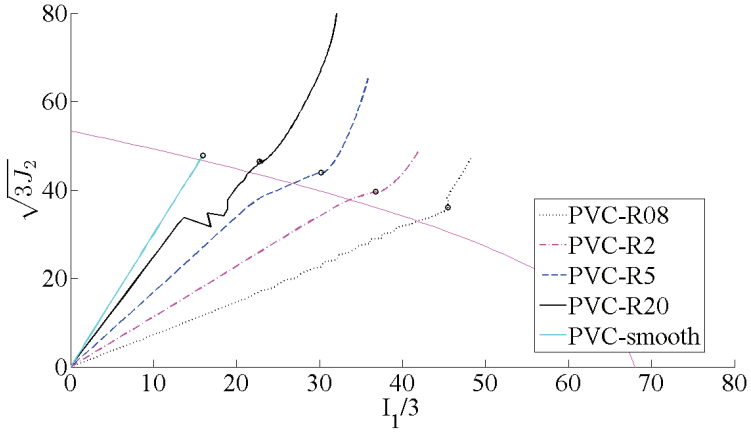

Figure 5.14: Yield Surface for PVC Simulations

5.1.5 Volume Strain

The volume strain from the simulations and the tests are compared in Figures 5.15 and 5.16 for HDPE and Figures 5.17 and 5.18 for PVC.

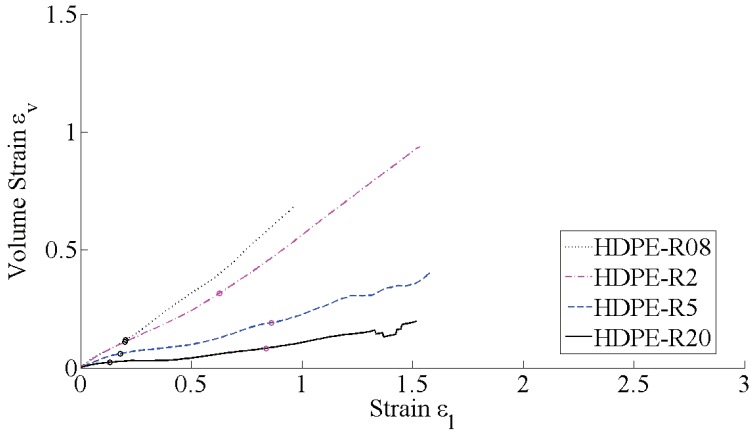

Figure 5.15: Volume Strain for HDPE Tests

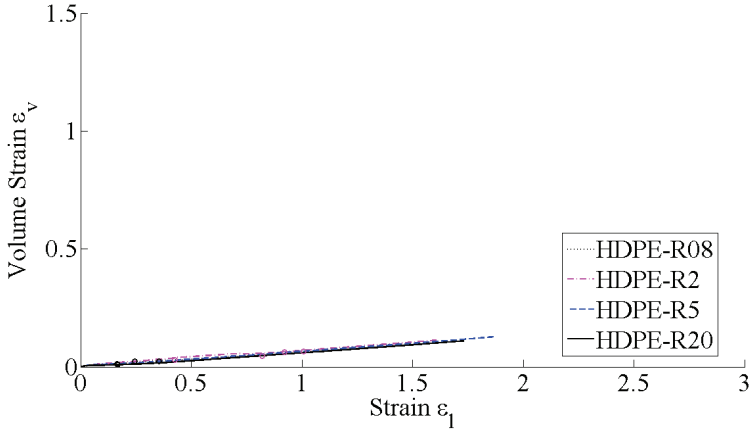

Figure 5.16: Volume Strain for HDPE Simulations

As can be seen, the deviations between the volume strain in the tests and in the simulations are relatively large. The volume strain is higher for the PVC simulations than the HDPE simulations because the material parameter β was set to be higher for PVC.

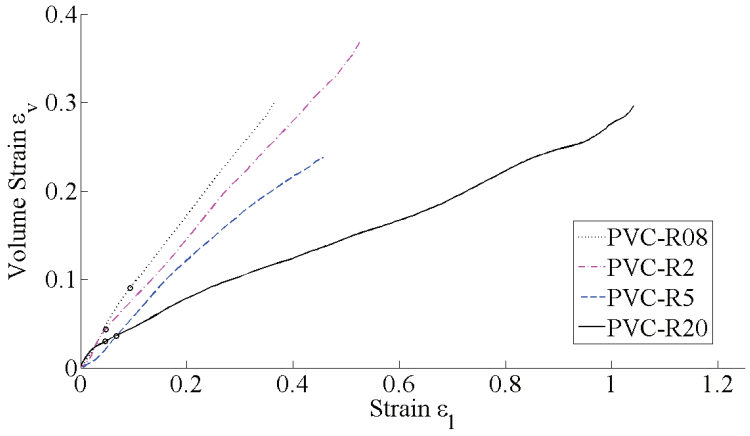

Figure 5.17: Volume Strain for PVC Tests

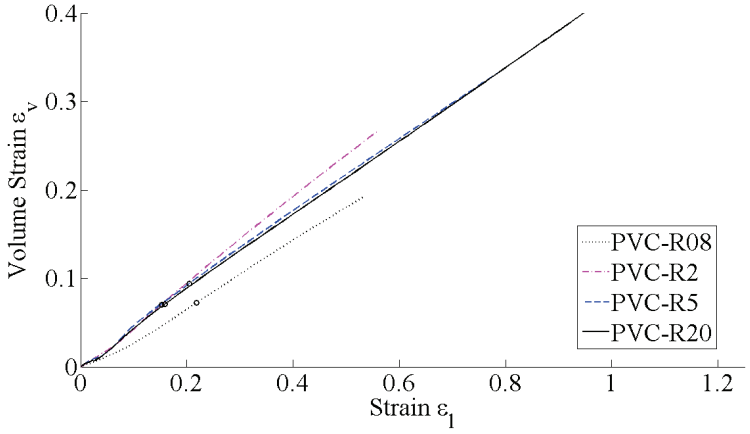

Figure 5.18: Volume Strain for PVC Simulations

From the experimental tests it is evident that the volume strain is dependent on the initial notch radius. A smaller initial notch radius gives a larger volume strain. This effect is due to the fact the specimens with smaller initial notch radii have a higher triaxiality and thus higher radial stress components. The specimens will then to a higher degree be stretched out in all three directions in the localised area, which will create greater void growth and thus greater volume changes. The variations in radial stress for the tests are shown in

Figures 5.19 and 5.20, where the radial stress is calculated as described in Section 2.3.

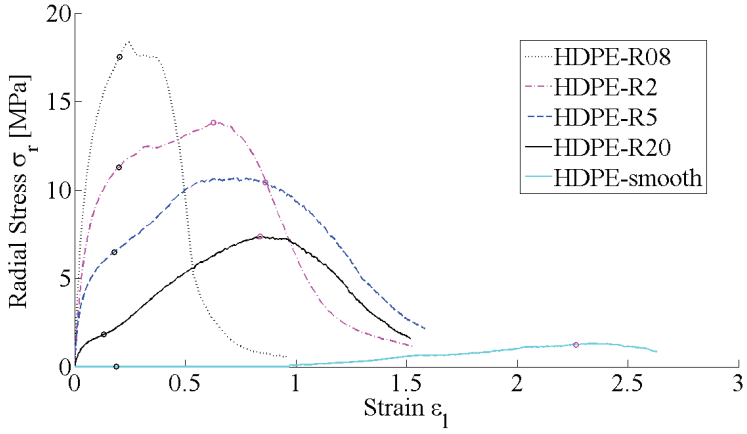

Figure 5.19: Radial Stress for HDPE Tests

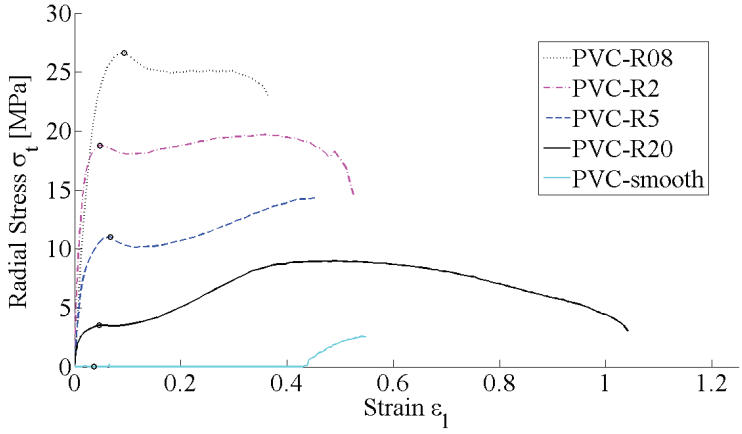

Figure 5.20: Radial Stress for PVC Tests

From the figures it can be seen that the smooth specimens will experience an uniaxial stress state initially. It can also be seen that increasing the initial notch radius gives a higher radial stress component. For HDPE the radial stress starts to sink around the point of cold drawing.

5.2 Evaluation of Tests and Simulations

From the information presented above it is evident that a smaller neck, and thus a larger triaxiality, leads to the following effects:

- A higher yield stress value, especially noticeable for HDPE
- A higher local strain rate
- Larger volume strain during plastic deformations
- Larger radial strain components

Figures 5.1 to 5.4 shows that more strain hardening is induced in the simulations than in the tests. The PVC experimental tests also had a larger stress drop after yielding than the PVC simulations. This larger drop in the tests might be due to the fact that the damage reduces the ability to carry load; as the voids grow the effective area is reduced. The area from which the stress is calculated is the area that can be measured from the outside of the specimen. In reality, the cross-section of the specimen will have a smaller area due to the void growth. For the tests the real stress σ_{eff} is

$$\sigma_{eff} = \frac{F}{A_{eff}} > \sigma = \frac{F}{A} \tag{5.1}$$

where $A = A_{eff} + A_{voids}$ is the area that can be measured from the outside of the specimen. Thus, the stress in the material surrounding the voids is actually higher than the plot shows. The load drop for the tests may also imply that there is an increase in void nucleation around yielding, and that the load drop occurs when nucleation around the particles present in the material happen. If this assumption is correct a stress driven nucleation criteria could be included, so that the void density f will change with the evolving stresses, to improve the material model further.

It was difficult to find the yield point for the simulations of the PVC specimens using the same method as for the tests, since the simulations did

not give a clear maximum on the true stress - true strain curve, as the tests did. Yielding may occur for a lower stress in reality, since the yield point found occurred after maximum load. However, it was chosen to still use the same method as in the tests for a better basis for comparison.

The yield point for the tests tends to be a bit lower than for the simulations, see Figures 5.11 to 5.14. Since the strain rates are similar, as shown in Figures 5.5 to 5.8, the yield point should also be similar. This indicates that the Raghava yield surface does not represent the exact material behaviour. The yield points for the simulations also tends to lie a bit above the purple line stretched as the yield surface. The reason for this is that this line applies to a theoretical zero strain rate. It can be seen that the specimens with the smaller initial notch radii has a yield point further from the yield surface than the larger radii. This is in accordance with the local strain rate varying with the initial notch radii, as shown in Figures 5.5 to 5.8.

For PVC the yield point can also be somewhat inaccurate because of the method used for determining the yield point not being very applicable for the simulations.

The volume strains predicted by the simulations, especially for HDPE, deviated from those observed in the experimental tests, see Figures 5.15 to 5.18. Clearly, the current material model, using the Raghava plastic potential, does not capture the volume changes that arises properly. It is believed that the GTN plastic potential, accounting for the void volume fraction f, will give a more correct material model when it comes to volume changes. The volume change is assumed to arise from void growth, which will be discussed further in Chapter 7.

Using the GTN model could also have made the yield surface for PVC curve more in accordance with the yield points, depending on the input parameters.

The volume strain in the simulation of PVC_R08 does not follow the same pattern as the other specimens. This is assumed to be a consequence of the volume strains being measured from different initial volumes V_0. Different

initial volumes V_0 may also give contributions to the deviations between the tests and simulations.

Accuracy of Longitudinal Strain and Volume Strain

It is assumed that the true longitudinal strain and the true volume strain are homogeneous over the area which they are calculated from. In reality, the strains will vary over the area. The true radial strain however, is calculated over an area with homogeneous strains. Comparing the longitudinal strain and the volume strain to the radial strain will therefore give an idea of how inhomogeneous the strain over the area from which the longitudinal strain and volume strain are calculated. It can also be a measure of the accuracy of the method employed for mapping the deformations.

The procedure for calculating the volume in order to find the volume strain ϵ_V, as described in Subsection 3.3.4, is rather demanding. Another way to calculate the volume strain ϵ_{v2} is using the trace of the finite strain tensor

$$\epsilon_{v2} = \epsilon_{11} + \epsilon_{22} + \epsilon_{33} = \epsilon_l + 2\epsilon_r \tag{5.2}$$

However, since the longitudinal strain is measured over a distance with varying radial strain and the radial strain is measured over a distance with uniform longitudinal strain, the longitudinal strain will not be as local as the radial. Thus, the radial and longitudinal strain will not be comparable, and will create a negative volume strain for some of the specimens. The method described in Subsection 3.3.4 is therefore preferable to use to find the volume.

To be able to compare the longitudinal strain and the volume strain to the radial strain, a mean radial strain was calculated. The mean radial strain is the radial strain taken over the area where the longitudinal strain is measured, calculated as

$$\epsilon_r = \frac{\epsilon_v - \epsilon_l}{2} \tag{5.3}$$

In Figures 5.21 and 5.22, the measured local radial strain and the mean radial strain from the tests are plotted together.

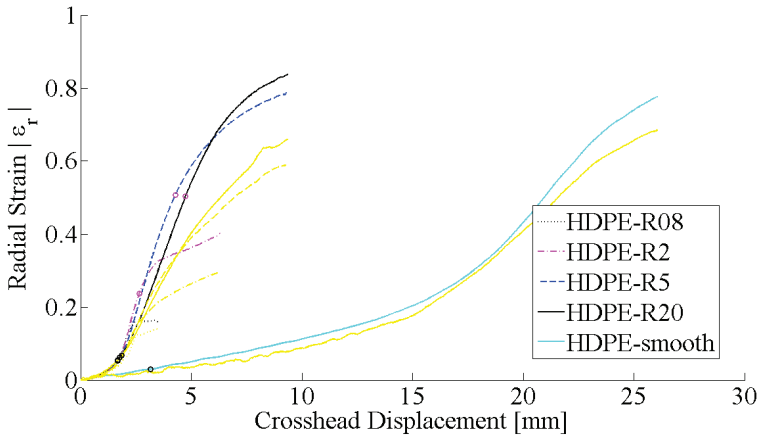

Figure 5.21: Local and Mean Radial Strain for HDPE tests

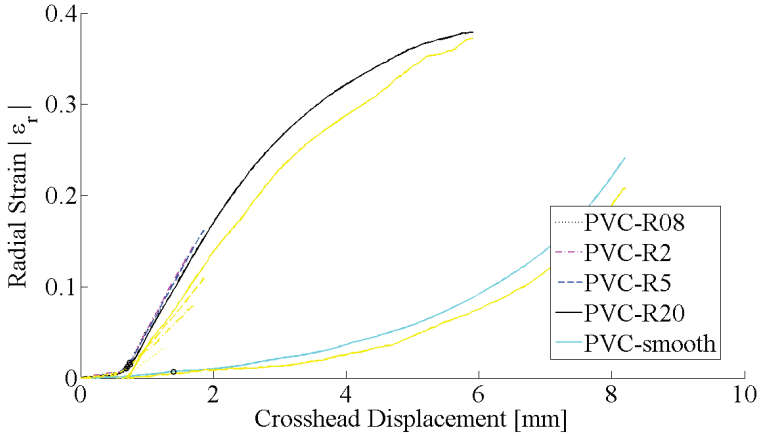

Figure 5.22: Local and Mean Radial Strain for PVC tests

Comparing the local and the mean radial strain gives an idea of the degree of localization and the accuracy of the longitudinal strain and the volume strain. As can be seen, the difference between the measured local radial strain and the mean radial strain increases with decreasing initial notch radius. This is due to the fact that for a specimen with a small initial notch radius the

diameter varies more over the area where the longitudinal strain is measured, than for a specimen with a larger initial notch radius. Thus the radial strain will vary more too. For instance, the relationship between the smallest and the largest diameter over the measuring area for R08 is approximately 0.79, while for R20 it will be approximately 0.99.

6

Numerical Simulations with Modified Material Model

As described in Section 2.2.1, a modified version of the material model employing the GTN yield surface and plastic potential is suggested. In this chapter simulations using the modified version implemented in LS-DYNA are presented. This material model was still under development when the simulations were performed. Therefore, the simulations are only an indication of what needs to be done in order to complete the modified material model.

Only simulations on one material, PVC, were conducted to try out the modified material model. PVC was chosen over HDPE because a good estimate of the initial void volume fraction f_0 in PVC was already acquired at SIMLab. Simulations were also only performed for two geometries, R08 and R2. The specimens with the smallest initial notch radii were chosen because they had the highest stress triaxiality, and thus the highest volume strain.

6.1 Calibration

To be able to run simulations with the modified material model, the parameters in Tables 2.2 and 2.3 were needed as input.

The parameters E and ν were already calibrated by Hovden [2010], and could be used to find E_0 and ν_0 solving the set of Equations (2.25) and (2.26) numerically. σ_0 and φ was found solving the set of Equations (2.16) and (2.17) numerically, using the values for σ_T and σ_C found by Hovden [2010]. The parameter φ was set equal to zero to make the material model easier to calibrate. This could be done because the only states of stress that would be investigated were the ones located between tension and biaxial tension. σ_T was also somewhat adjusted to get a better approximation for the yield stress, since the parameter g, which affects the yield stress, was not accurately calibrated for the simulations.

Further, the parameters $\dot{\epsilon}_{0A}$, C, C_R and $\bar{\lambda}_L$ were also already calibrated by Hovden [2010], and could be used directly.

The parameter g was set to be $g = 1$, and h was set equal to g. q was set to be $q = 1$, as suggested by Delhaye [2010]. f_0 was set to be $f_0 = 0.2$, a value estimated at SIMLab from micrographs of PVC. The parameters are summed up in Table 6.1.

Table 6.1: Set of Calibrated Parameters for PVC

$\dot{\epsilon}_{0A}$	0.001
C	0.07
E_0	4500
ν_0	0.3263
σ_0	55
h	1
g	1
q	1
φ	0
f_0	0.2
C_R	5.5
$\bar{\lambda}_L$	1.92

In addition H, the bulk modulus K, the shear modulus G and the retraction coefficient R were needed as input for the material model in LS-DYNA. H was set equal to zero, and $K = 2500$ and $R = 0.32$ were taken from Hovden [2010]. G was adjusted up to $G = 4142$, to increase the stability of the model.

To adjust the parameters, analyses on a single element model and on the notched specimens PVC_R08 and PVC_R2 were performed.

6.2 Results

The true stress - true strain curves for the tests and the simulations, with both the current and the modified material model, are compared in Figures 6.1 and 6.2.

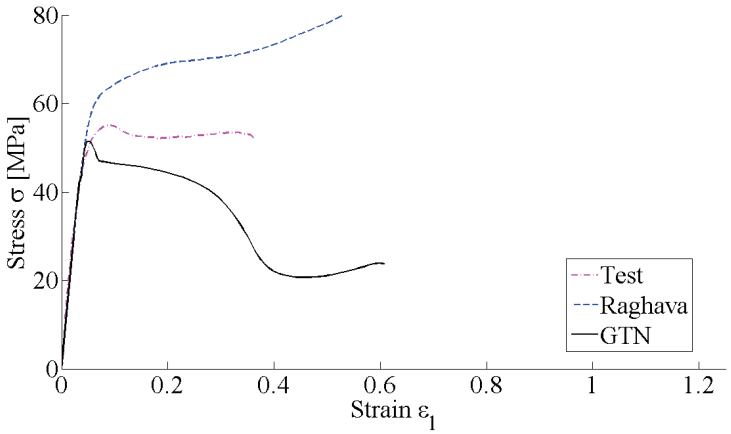

Figure 6.1: Comparison of True Stress - True Strain Curves for PVC_R08

The comparison shows that the softening in the modified material model is overestimated. The modified material model manages to model the fall in the stress value seen immediately after yielding in the tests, however the shapes of the drops are a bit different in the tests.

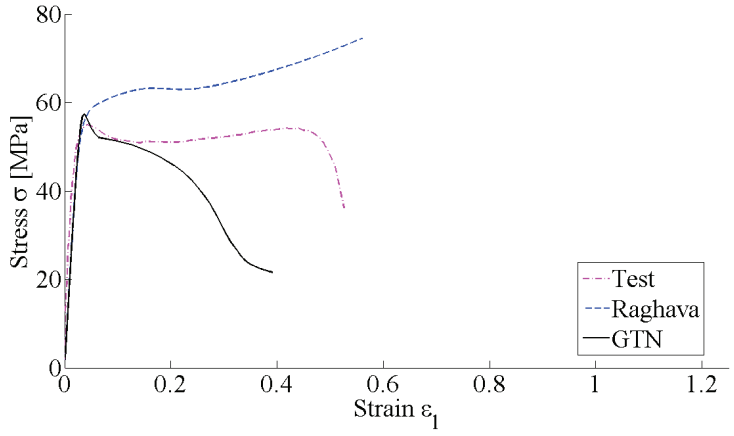

Figure 6.2: Comparison of True Stress - True Strain Curves PVC_R2

In Figures 6.3 and 6.4, the volume strain for the tests are compared to the volume strain for the simulations with both the current and the modified material model.

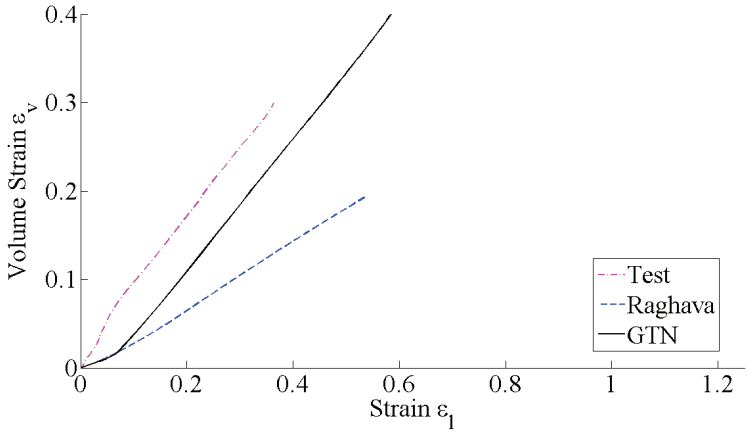

Figure 6.3: Comparison of Volume Strain Curves for PVC_R08

As can be seen, the GTN potential estimates the volume strain better than the Raghava potential. The volume strain gradient for PVC_R08 is similar for the simulation using the GTN potential and for the test. For PVC_R2 the volume strain gradient is a bit steeper in the simulation using

the GTN potential than in the test. The simulated volume strain for longitudinal strains lower than approximately 0.07 deviate from the tests.

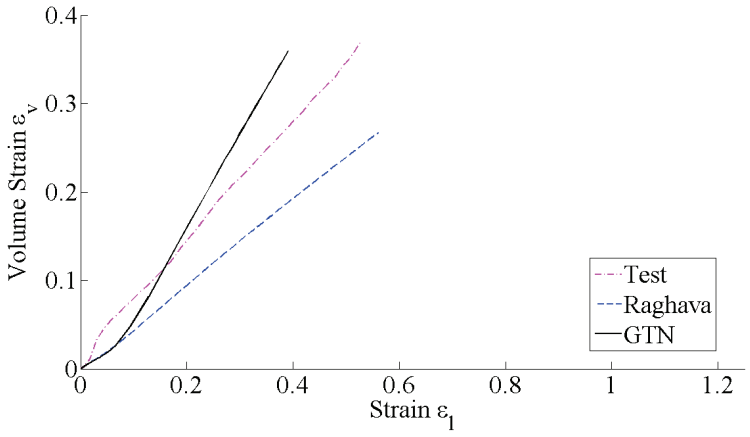

Figure 6.4: Comparison of Volume Strain Curves for PVC_R2

6.3 Evaluation of Modified Material Model

The modified material model captures the volume changes that arises in polymer materials exposed to strain better than the current one. The GTN plastic potential will thus give a more correct material model. However, the strain softening is not yet simulated properly. The volume strain gradient should also be adjusted by approximating a better value for the parameter g using the volume strain in uniaxial tension tests.

In order to simulate the strain softening properly, the parameters from part B, C_R and $\bar{\lambda}_L$ should be adjusted to get the correct level of strain hardening at the end of the test. Adjustments of the parameters needs to be done because Part A exhibits softening during plastic deformation in the modified material model, instead of a plateau as with the original model, so the strain softening can be overestimated.

A problem that occurred while running simulations with the modified material model, was numerical instability. The instability was caused by mass scaling, which was introduced to reduce the CPU time. Since the analysis was so sensitive to mass scaling, only scaling of a factor 10^3 could be used. This gave a very long CPU time, and consequently the analyses were rather time consuming to perform.

7

Fracture Criterion and Fracture Surfaces

Examining fractures and fracture surfaces can give useful information about the fracture process and the failure cause.

In this chapter first a plot of equivalent plastic fracture strain from the tests is shown. Further the fractures and fracture surfaces from the tests are described and evaluated.

7.1 Equivalent Plastic Fracture Strain

The equivalent plastic fracture strain p_f, found as described in Section 2.4, is plotted against the triaxiality ratio at fracture in Figure 7.1.

As can be seen the smaller the neck, the lower the equivalent plastic fracture strain.

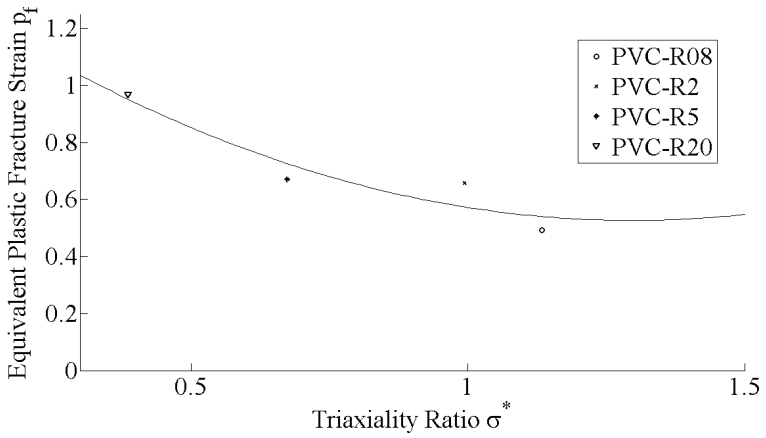

Figure 7.1: Equivalent Plastic Fracture Strain for PVC Specimens

7.2 Fracture Surface

To examine the fracture surface of the specimens from the tension tests, a Canon 40D single-lens reflex (SLR) camera with a high definition lens and two external light sources was used. The results are shown in the following.

During the testing, all PVC specimens fractured. For HDPE, only HDPE_R08 and HDPE_R2 fractured.

7.2.1 Results

In Figure 7.2 the fracture surface of HDPE_R2 is shown. As can be seen, the voids are relatively large in the centre of the specimen. Presumably this is where the void growth started, and then propagated from these voids out to the outer shell. This is in accordance with the theory of Bridgman, Equation (2.37); the centre region is where the highest stress triaxiality is present, and therefore the region most exposed for void growth.

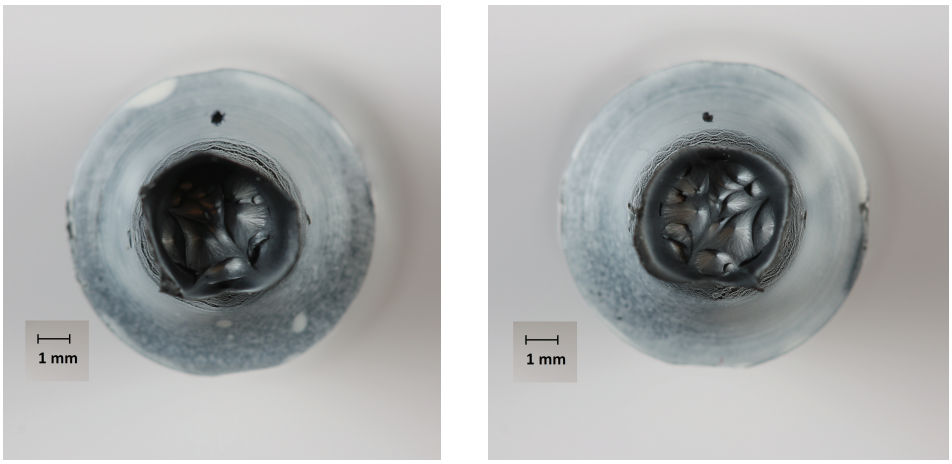

Figure 7.2: Fracture Surface of HDPE_R2

In Figure 7.3 the fracture surface of PVC_R2 is shown. Clearly, PVC have smaller voids than HDPE. The fracture surface also looks as though the fracture process was less ductile for PVC due to the length of the fibrils on the surface.

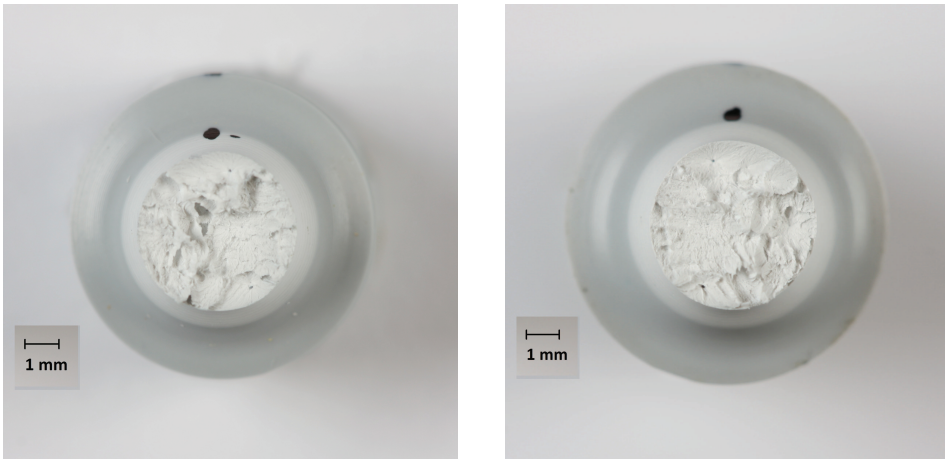

Figure 7.3: Fracture Surface of PVC_R2

Comparing the fracture surfaces from the tests for PVC it was seen that the lower the initial notch radius, the more topographic the fracture surface,

see Figure 7.4. Thus, higher triaxiality leads to more brittle fractures.

(a) PVC_R08 (b) PVC_R20

Figure 7.4: Differences in Topography due to Triaxiality

Looking at Figure 7.5, where pictures taken some seconds after yielding are shown, it can be seen that local whitening of the material has occurred. As described in Section 2.5, this is a sign of cavitation.

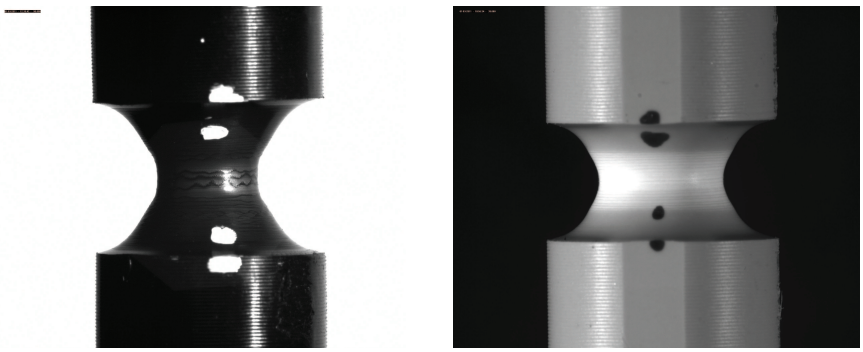

(a) HDPE_R2 (b) PVC_R2

Figure 7.5: Local Whitening of the Material due to Void Growth

7.3 Evaluation

From the information presented above it is evident that a smaller neck, and thus a larger triaxiality, leads to the following effects for PVC:

- A lower equivalent plastic fracture strain
- A less topographic fracture surface

It was seen that there were voids present on the fracture surfaces for both HDPE and PVC. This is in accordance with the volume changes that were registered in the tests, and the assumption that volume change is due to void growth.

8

Conclusions

The post-processing of the tests, using the custom made DIC algorithm outlined in Subsection 3.3.4, showed results in agreement to the hand measurements conducted in ImageJ. Also, the comparison of the local with the mean radial strain in Figures 5.21 and 5.22, showed manageable deviations between the two, and thus a good enough degree of localisation of the longitudinal strain and volume strain. The developed algorithm is therefore a good way to post-process the tests, avoiding the earlier stated problems, and giving accurate results.

From the tests and simulations, the triaxiality was found to affect several parameters. A smaller neck, and thus a larger triaxiality, leads to the following:

- A higher yield stress value, especially noticeable for HDPE
- A higher local strain rate
- Larger volume strain during plastic deformations
- Larger radial strain components
- A lower equivalent plastic fracture strain for PVC
- A less topographic fracture surface for PVC

It is clear that voids nucleate in both HDPE and PVC in tension, this causes volume change. Both visual whitening of the test specimens right after yielding and voids at the fracture surfaces supports this assumption.

The simulations where the Raghava potential was used showed that volume change could not be predicted properly. The Raghava yield surface and plastic potential could therefore be replaced with the GTN, as a modification of the material model as suggested by Delhaye [2010]. However, obtaining the initial void volume fraction of a material is a rather extensive process, and the modified material model will thus be more demanding to calibrate. If simple calibration is the most desired quality, the Raghava yield surface and plastic potential will be preferable.

The testing of the material model employing the GTN yield surface and plastic potential showed that the volume strain now is far better estimated. However, the simulations overestimated the strain softening, and adjustments of the B part has to be made.

Recommendations for further work

The modified material model needs to be adjusted to get the correct level of strain softening. Also, all the parameters for the model should be properly calibrated for all the relevant thermoplastics.

A stress driven nucleation criteria should be tested, since it is believed that the load drop on the stress - strain curves is caused by a sudden increase in nucleation around yielding.

References

Anand, L. (1996). A constitutive model for compressible elastomeric solids. *Computational Mechanics*, **18**, 339-355.

Arruda, E., Boyce, M., and Jayachandran, R. (1995). Effects of strain rate, temperature and thermomechanical coupling on the finite strain deformation of glassy polymers. *Mechanics of materials*, **19**, 193-212.

Bao, Y. and Wierzbicki, T. (2004). On fracture locus in the equivalent strain and stress triaxiality space. *International Journal of Mechanical Sciences*, **46**, 81-98.

Belytschko, T., Liu, W. K., and Moran, B. (2000). *Nonlinear Finite Elements for Continua and structures*. John Wiley & Sons Ltd.

Bois, P. D., Kolling, S., Koesters, M., and Frank, T. (2005). Material behaviour of polymers under impact loading. *International Journal of Impact Engineering*, **32**, 725-740.

Boyce, M. C., Socrate, S., and Llana, P. (2000). Constitutive model for the finite deformation stress - strain behaviour of poly(ethylene terephtalate) above the glass transition. *Polymer*, **41**, 2183-2201.

Bridgman, P. W. (1964). *Studies in Large Plastic Flow and Fracture*. Harvard University Press, Cambridge, Massachusetts.

Clausen, A. H., Børvik, T., Hopperstad, O. S., and Benallal, A. (2003). Flow and fracture characteristics of aluminium alloy aa5083-h116 as function of strain rate, temperature and triaxiality. *Materials Science and Engineering*, **364**, 260-272.

Delhaye, V. (2010). *Behaviour and modelling of polymers for crash applications*. PhD thesis, Norwegian University of Science and Technology.

Delhaye, V., Clausen, A. H., Moussy, F., Hopperstad, O. S., and Othman, R. (2010). Mechanical response and microstructure investigation of a mineral and rubber modified polypropylene. *Polymer Testing*, **29**, 793-802.

Dupaix, R. and Boyce, M. (2007). Constitutive modelling of the finite strain behaviour of amorphous polymers in and above the glass transition. *Mechanics of materials*, **39**, 39-52.

Engel, L., Klingele, H., Ehrenstein, G. W., and Schaper, H. (1981). *An Atlas of Polymer Damage*. Wolfe Publishing Ltd, London.

G'Sell, C., Hiver, J., Dahoun, A., and Souahi, A. (1992). Video-controlled tensile testing of polymers and metals beyond the necking point. *Journal of materials science*, **27**, 5031-5039.

Gurson, A. L. (1977). Continuum theory of ductile rupture by void nucleation and growth: Part I - yield criteria and flow rules for porous ductile media. *Journal of Engineering Materials and Technology*, **99**, 2-15.

Hovden, M. T. (2010). Tests and numerical simulations of polymer components. Master's thesis, SIMLab, NTNU.

Kamaya, M. and Kawakuboa, M. (2011). A procedure for determining the true stress - strain curve over a large range of strains using digital image correlation and finite element analysis. *Mechanics of Materials*, **43**, 243-253.

Lemaitre, J. and Chaboche, J.-L. (1990). *Mechanics of Solid Materials*. Cambridge University Press, Cambridge, United Kingdom.

Lemaitre, J. and Desmorat, R. (2005). *Engineering Damage Mechanics - Ductile, Creep, Fatigue and Brittle Failures*. Springer-Verlag Berlin Heidelberg.

LSTC (2007). LS-DYNA Keyword Users Manual, version 971. Livermore Software Technology Corporation.

McCrum, N. G., Buckley, C. P., and Bucknall, C. (1997). *Principles of Polymer Engineering*. Oxford University Press.

Mirone, G. (2006). Role of stress triaxiality in elastoplastic characterization and ductile failure prediction. *Engineering Fracture Mechanics*, **74**, 1203-1221.

Morawiec, J., Bartczak, Z., Kazmierczak, T., and Galeski, A. (2001). Rolling of polymeric materials with side constraints. *Materials Science and Engineering A*, **317**, 21-27.

Pijnenburg, K. and Van der Giessen, E. (2001). Macroscopic yield in cavitated polymer blends. *International Journal of Solids and Structures*, **38**, 3575-3598.

Polanco-Loria, M., Clausen, A. H., Berstad, T., and Hopperstad, O. S. (2010). Constitutive model for thermoplastics with structural applications. *International Journal of Impact Engineering*, **37**, 1207-1219.

Raghava, R., Caddell, R. M., and Yeh, G. S. Y. (1973). The macroscopic yield behaviour of polymers. *Journal of materials science*, **8**, 225-232.

Ram, A. (1997). *Fundamentals of Polymer Engineering*. Plenum Press, New York.

Rösler, J., Harders, H., and Bäker, M. (2007). *Mechanical Behaviour of Engineering Materials - Metals, Ceramics, Polymers, and Composites*. Springer-Verlag Berlin Heidelberg.

SIMONA-AG (1995). Product information PE-HWU/PE-HWST.

SIMONA-AG (1996). Product information PVC-TF.

Steenbrink, A. and Van der Giessen, E. (1999). On cavitation, post cavitation and yield in amorphous polymer-rubber blends. *Journal of the Mechanics and Physics of Solids*, **47**, 843-876.

Tvergaard, V. and Needleman, A. (1983). Analysis of the cup-cone fracture in a round tensile bar. *Acta Metall*, **32**, 157-169.

Vincent, P. I. (1959). The necking and cold-drawing of rigid plastics. *Polymer*, **1**, 7-19.

Zhang, Z. L. and Niemi, E. (1995). A class of generalized mid-point algorithms for the Gurson-Tvergaard material model. *International Journal for Numerical Methods in Engineering*, **38**, 2033-2053.

A

Appendix A

Representative MATLAB Code used in Post-Processing of Tests

```
%%%%%%%%%%%%%%%%%%%%%%%%%%%%%%%%%%%%%%%%%%%%%%%%%%%%%%%%%%%%%%%%%%%%%%%%%%%%%%%%
%                               IMAGE PROCESSOR                                %
%                                   PVC_R2                                     %
%%%%%%%%%%%%%%%%%%%%%%%%%%%%%%%%%%%%%%%%%%%%%%%%%%%%%%%%%%%%%%%%%%%%%%%%%%%%%%%%

clc
clear all
close all

%set a fatter linewidth to make lines and dots more visable
set(0,'defaultlinelinewidth',2)

%find all files in the current folder with the extension *.bmp
files = dir('*.bmp');

%create storage space vectors
l=length(files);
h = zeros(l,1);
v = zeros(l,1);
d = zeros(l,1);
r=zeros(l,1);

%assign the number of points that is going to be found on the contour of the
%specimen to calculate the radius
```

```
num_points=300;
%assign a threshold value.
%Try different threshold values for a better contrast in the images
threshold=0.18;
%if the specimen isn't properly centered, use moved to adjust
movedx=-10;
movedy=0;
%show the first picture and use the data cursor to find start of contour search:
%The x-value=leftcol and the y-value=bottomrow
leftcol=708;
bottomrow=1300;
%Use bottomrowset if the position of bottomrow needs to move for every picture
bottomrowset=bottomrow;

%set a minimum diameter, height and radius in pixels to avvoid error measurements
dmin=600;
hmin=200;
rmin=dmin/2;

%guess an approximate centre and radius of the first
%optimized circle in the specimens notch in pixels [y0 x0 r]
P0 = [1158 556 260];

%assign a value to be used for adjustments of other values
desi=0;

%tell MATLAB which pictures to include
start=0;
stop=100;

%use the method VolumeAndHeight on all the files found.
%The method VolumeAndHeight is included later.
for i=1:l
if i <= stop && i>start
filename = files(i).name;
I = imread(filename);
[height,volume,diam,contour]=
VolumeAndHeight(I,num_points,threshold,movedx,movedy,bottomrow,leftcol,dmin,hmin,rmin);
h(i) = height;
v(i) = volume;
d(i)=diam;

%write out the number of the current picture
i

end

%adjustment of values as pictures are changing during a test
num_points=num_points-1;
desi=desi+1.8;
```

A2

```
bottomrow=round(bottomrowset-desi);


%use a least square routine to find an optimized circle fitting the contour
%with the method OptimCircle. Optim Circle is included later.
 if i <= stop && i>start
P = lsqnonlin(@OptimCircle,P0,[],[],[],contour);

%plot the circle
theta = 0:0.01:2*pi;
x = P(3)*cos(theta) + P(2);
y = P(3)*sin(theta) + P(1);
plot(x,y,'m')

%set a new center and radius for the start of the next circle optimization
P0 = [P(1) P(2) P(3)];
%store the radius
r(i)=P(3);
end
end

%convert pixels to mm. The relationship between them is found using ImageJ
mmINpx=0.007188;
h=smooth(h*mmINpx,10);
v=smooth(v*mmINpx^3,10);
d=smooth(d*mmINpx,10);
r=smooth(r*mmINpx,10);

%write height, volume, diameter and radius to an excel sheet output.xls
out=[h,v,d,r];
xlswrite('output.xls',out,'Output')



%%%%%%%%%%%%%%%%%%%%%%%%%%%%%%%%%%%%%%%%%%%%%%%%%%%%%%%%%%%%%%%%%%%%%%%%%%%%%%%
%                                VolumeAndHeight                               %
%%%%%%%%%%%%%%%%%%%%%%%%%%%%%%%%%%%%%%%%%%%%%%%%%%%%%%%%%%%%%%%%%%%%%%%%%%%%%%%

function[height,volume,diam,contour]=
VolumeAndHeight(I,num_points,threshold,movedx,movedy,bottomrow,leftcol,dmin,hmin,rmin)

%make image black-white
BW = im2bw(I,threshold);

%invert colours for HDPE
%BW=~BW;

%hold an image to plot all points found
figure(1)
imagesc(BW)
```

```
colormap gray
hold on

%zoom in on picture if necessary
%axis([800 1500 700 1400])

%Find the starting point for the contour
%whites gives the positions of white pixels in a row
whites = find(BW(bottomrow,:));
%id gives all the elements in whites to the right of leftcol an id-number
id = find(whites > leftcol);
%the column with the first id-number is where the search is supposed to begin.
white1 = whites(id(1));
%plot the starting point for the search
plot(white1,bottomrow,'c*')

%Find the contour of the specimen
connectivity = 8;
contour =
bwtraceboundary(BW,[bottomrow, white1],'N',connectivity,num_points);
%smooth the contour
contour(:,2) = smooth(contour(:,2),50);
contour(:,2) = round(contour(:,2));
%plot the contour
plot(contour(:,2),contour(:,1),'c','LineWidth',2);

%the least diameter can be found where contour(:,2) has its largest value
[xneck, elxneck]=max(contour(:,2));
ymid=(contour(elxneck,1))+movedy;
%plot where the diameter search is supposed to start
plot(xneck,ymid,'c*')

%find the centre and the smallest diameter of the specimen
i=xneck;
j=ymid;
diam=0;
while BW(j,i)==1 || diam<dmin
    diam=diam+1;
    i=i+1;
end

%plot the point where the diameter measurement stops to check if its correct
plot((xneck+diam),ymid,'c*')

%plot where the search for the length between the black dots should start
xextenso=round(xneck+diam/2)+movedx;
plot(xextenso,ymid,'g*')

%Find the nearest black dot on the specimen, up
i=xextenso;
```

```
j=ymid;
heightu=0;

while BW(j,i)==1||heightu<hmin
    heightu=heightu+1;
    j=j-1;
end
plot(xextenso,ymid-heightu,'b*')

%Find the nearest black dot on the specimen, down
i=xextenso;
j=ymid;
heightd=0;

while BW(j,i)==1||heightu<hmin
    heightd=heightd+1;
    j=j+1;
end
plot(xextenso,ymid+heightd,'b*')

%Find radiuses from the middle and up to the nearest black dot
radiu=zeros(heightu,1);
r=0;
xmid=round(xneck+diam/2);
xmids=xmid;
ymids=ymid;
for n=1:heightu

    while BW(ymids,xmids)==1 || r<rmin
    r=r+1;
    xmids=xmids-1;
    end

 xmids=xmid;
 ymids=ymids-1;
 radiu(n)=r;
 r=0;
end
plot(xmid-radiu(1),ymid,'c*')

%Find radiuses from the middle and down to the nearest black dot
radid=zeros(heightd-1,1);
r=0;
xmids=xmid;
ymids=ymid+1;

for n=1:heightd-1

    while BW(ymids,xmids)==1 || r<rmin
    r=r+1;
```

```
    xmids=xmids-1;
    end

 xmids=xmid;
 ymids=ymids+1;
 radid(n)=r;
 r=0;
end
plot(xmid-radid(1),ymid,'c*')

%Find the volume of the region between the black dots
volume=0;
for i=1:heightu-1
    volume=volume+(0.5*(radiu(i)+radiu(i+1)))^2*pi;
end

for i=1:heightd-2
    volume=volume+(0.5*(radid(i)+radid(i+1)))^2*pi;
end

%Find the height, thus the distance between the nearest dots
height=(heightu+heightd);

end
```

```
%%%%%%%%%%%%%%%%%%%%%%%%%%%%%%%%%%%%%%%%%%%%%%%%%%%%%%%%%%%%%%%%%%%%%%%%%%%%%%%%
%                                  OptimCircle                                  %
%%%%%%%%%%%%%%%%%%%%%%%%%%%%%%%%%%%%%%%%%%%%%%%%%%%%%%%%%%%%%%%%%%%%%%%%%%%%%%%%

function F = OptimCircle(P,contour)

xc = P(1);
yc = P(2);
r = P(3);

for i = 1:length(contour(:,2))
    s = sqrt(power(xc-contour(i,1),2)
    + power(yc-contour(i,2),2));
    F(i) = abs(s-r);
end
end
```

B

Appendix B

Tension Tests on Circumferentially Notched Specimens

In this appendix the test setup and the basic results of tension tests on axisymmetric smooth and notched specimens performed at the Department of Structural Engineering at NTNU in January and March 2011 are presented.

Test Setup and geometry of specimens

The notched specimens had four different notch radii, $R = 0.8mm$, $R = 2mm$, $R = 5mm$ and $R = 20mm$, in addition to the smooth one. Each of the different specimens were made in both PVC and HDPE, giving a total of ten tests. Both materials were made by SIMONA AG, Germany. The specimens were named on the form (material)_R(radius)_(test no.), e.g. for the first test of a PVC specimen with $R = 2mm$, the name would be PVC_R2_1. The smooth specimens were named as (material)_smooth_(test no.).

In figure B.1 the geometries of the test specimens are shown. The geometry of the smooth specimens are shown to the left, and the geometry of the other specimens to the right.

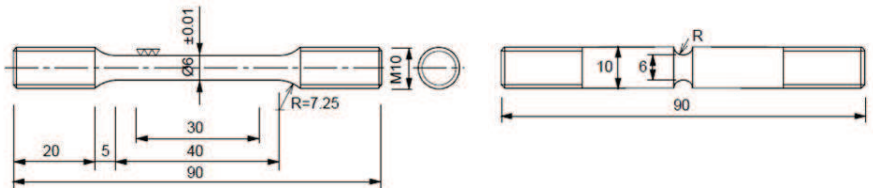

Figure B.1: Geometry of Test Specimens

The tests were performed using a Dartec M 1000 RK machine with a 20 kN load cell, see figure B.2(a), connected to an Instron controller, see figure B.2(b).

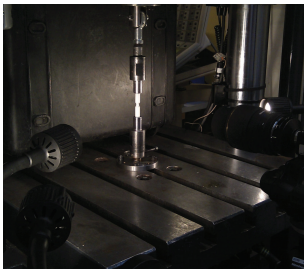

(a) Dartec Machine

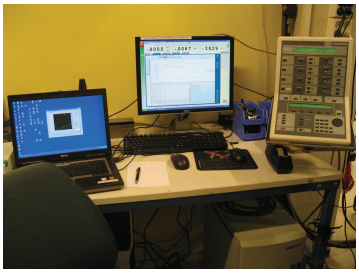

(b) Instron Controller

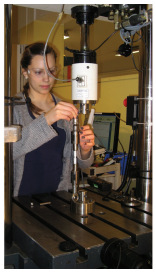

(c) Mounting

Figure B.2: Laboratory Testing

Results

For each test pictures of the specimens before deformation and under deformation are shown. Also, force - crosshead displacement curves for all three test rounds, and true stress - true strain curves from test set no. 3, is given. In addition the key data presented in figure B.3 and table B.1 is given for each of the PVC tests. Pictures of the fracture surfaces from one of the test sets are also shown.

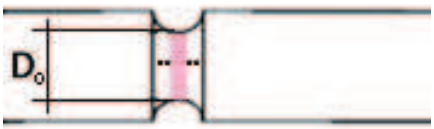

Figure B.3: Initial Diameter D_0

Table B.1: Key Data

D_0	Initial diameter
$D_\perp$	Diameter immediately after fracture, perpendicular to $d_\parallel$
$D_\parallel$	Diameter immediately after fracture, perpendicular to $d_\perp$

HDPE_R08

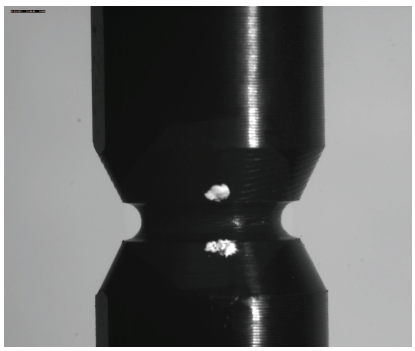

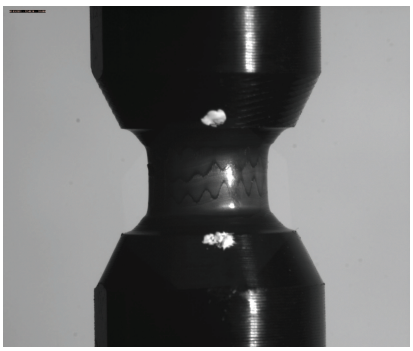

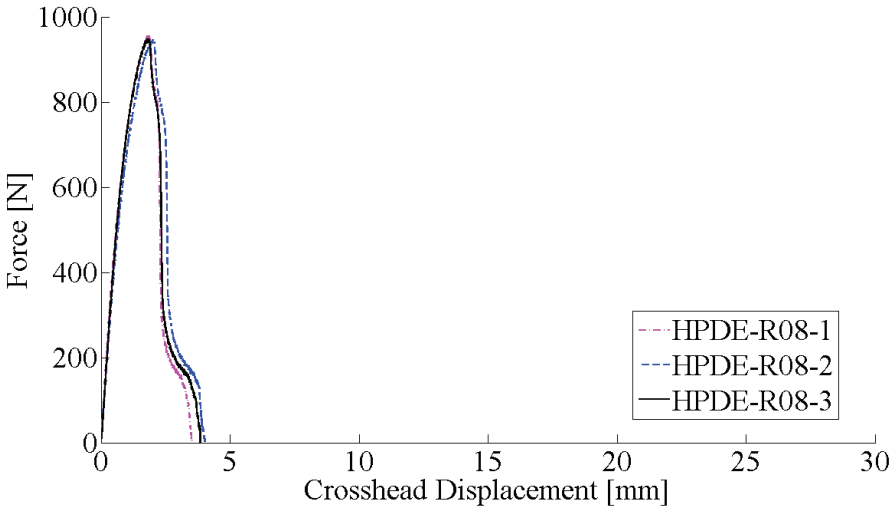
1000
800
600
400
200
0
Force [N]
0
5
10
15
20
25
30
Crosshead Displacement [mm]
HPDE-R08-1
HPDE-R08-2
HPDE-R08-3

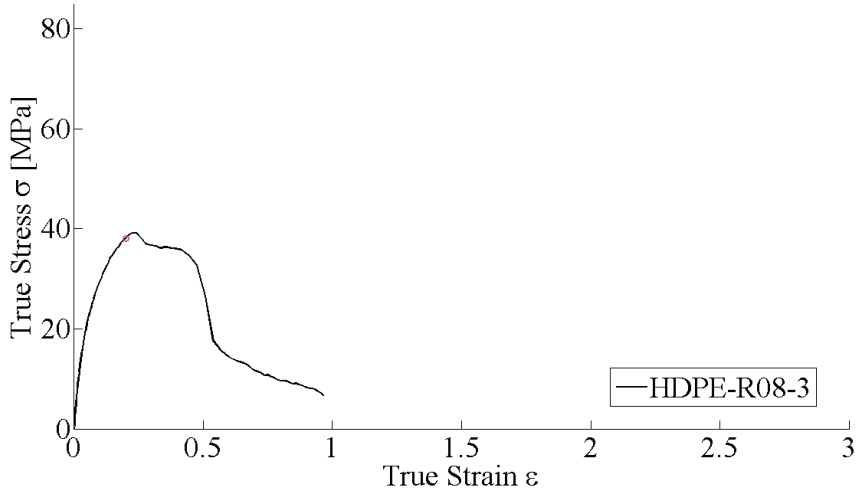
True Stress σ [MPa]
80
60
40
20
0
0
0.5
1
1.5
2
2.5
3
True Strain ε
HDPE-R08-3

HDPE_R2

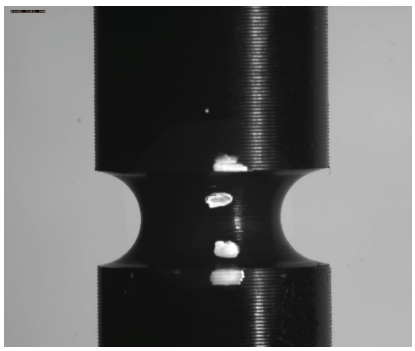

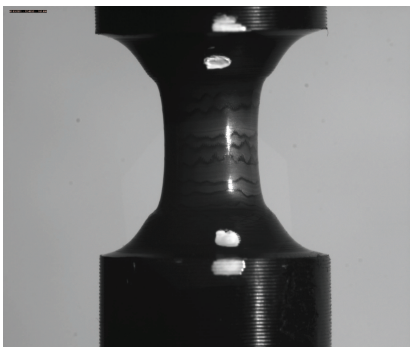

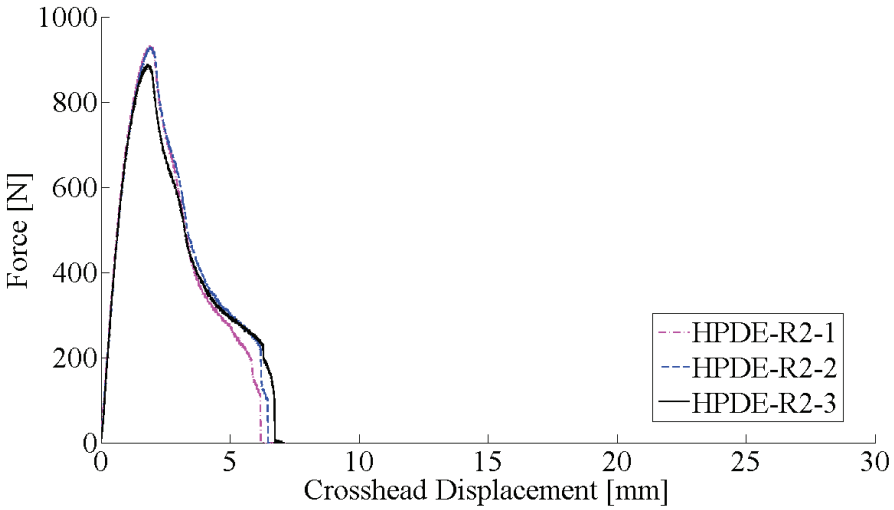
1000
800
600
400
200
0
Force [N]
0
5
10
15
20
25
30
Crosshead Displacement [mm]
HPDE-R2-1
HPDE-R2-2
HPDE-R2-3

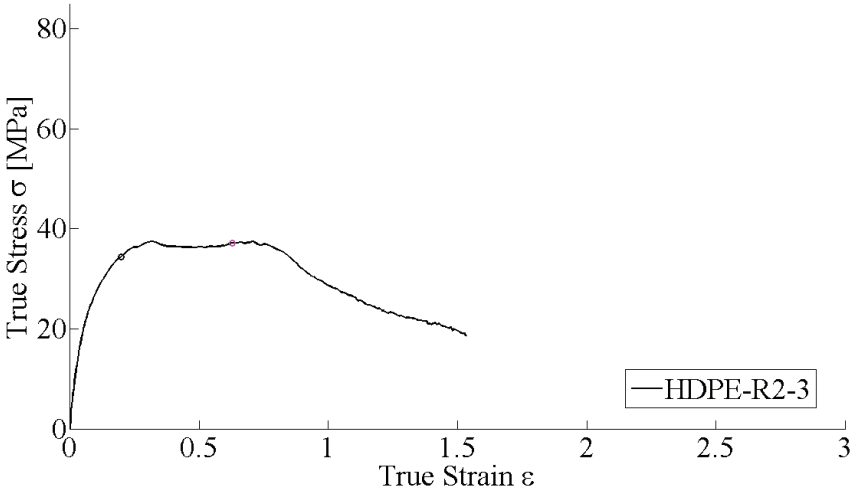
True Stress σ [MPa]
80
60
40
20
0
0
0.5
1
1.5
2
2.5
3
True Strain ε
HDPE-R2-3

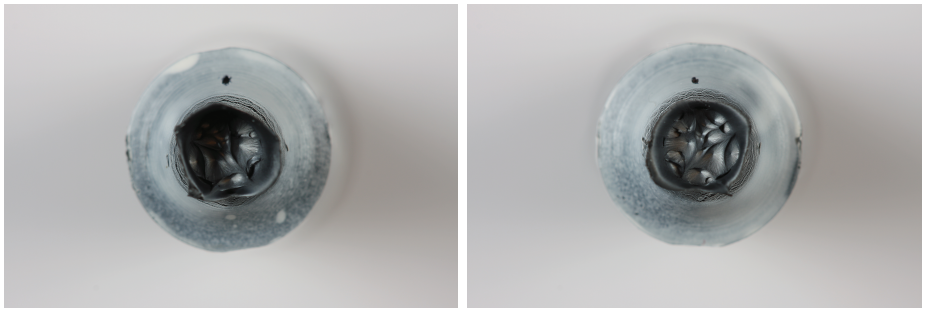

HDPE_R5

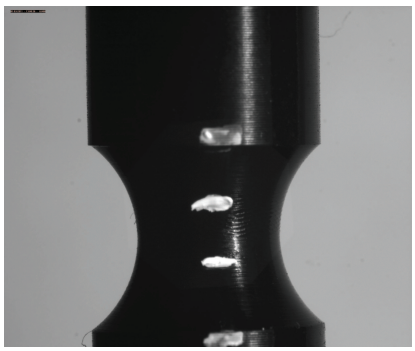

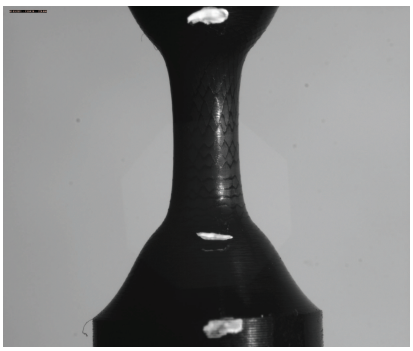

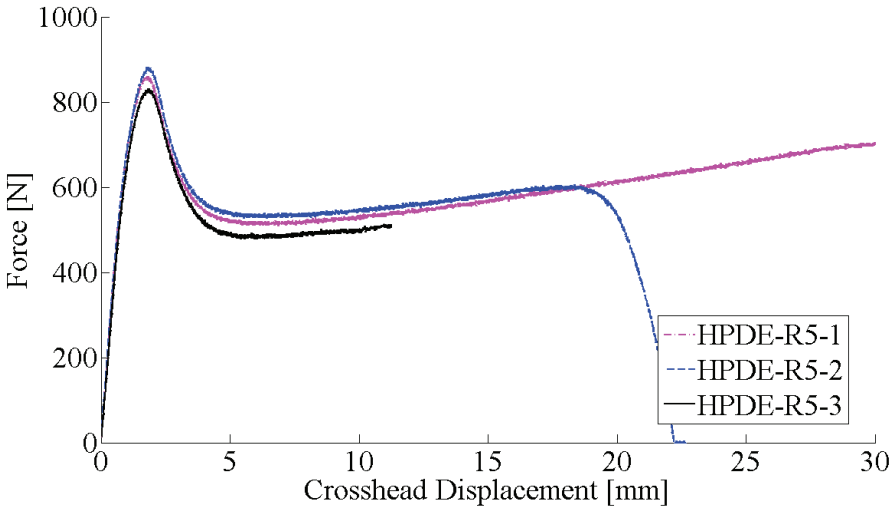

Comments: The specimens did not fracture.

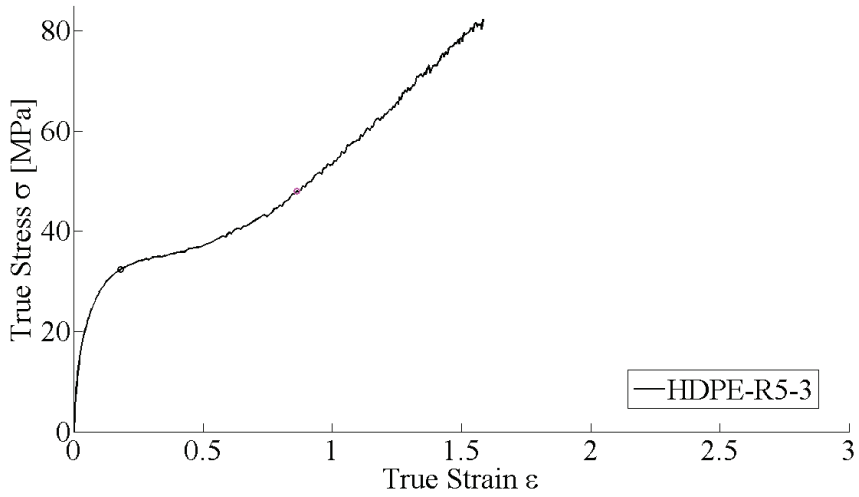
True Stress σ [MPa]
True Strain ε
HDPE-R5-3
0
20
40
60
80
0
0.5
1
1.5
2
2.5
3

HDPE_R20

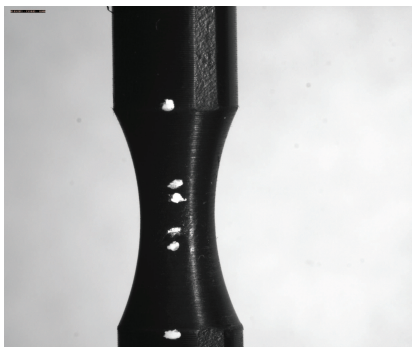

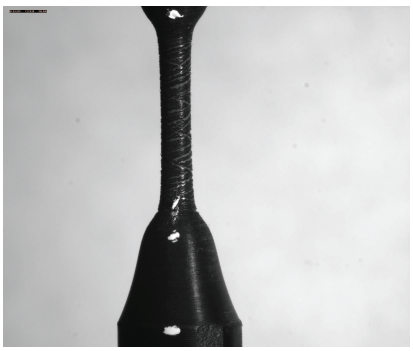

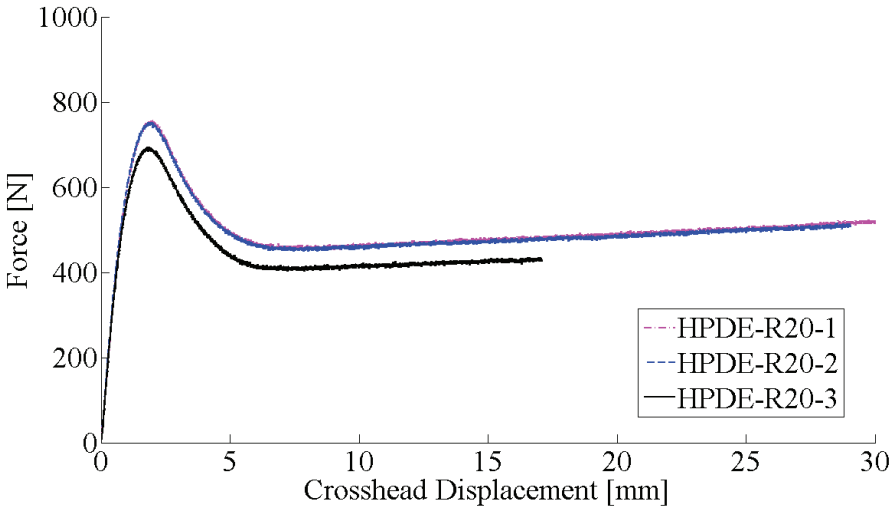

Comments: The specimens did not fracture.

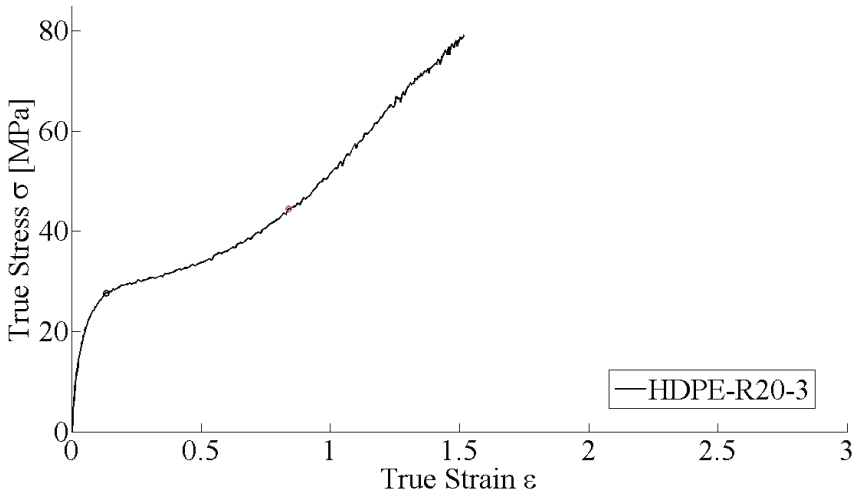
True Stress σ [MPa]
True Strain ε
HDPE-R20-3
0
20
40
60
80
0
0.5
1
1.5
2
2.5
3

HDPE_smooth

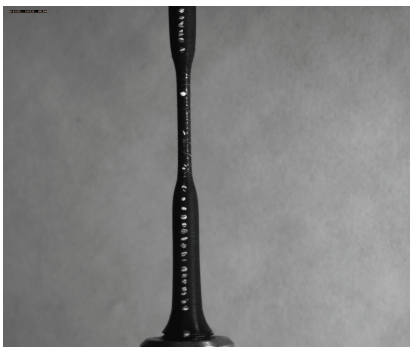

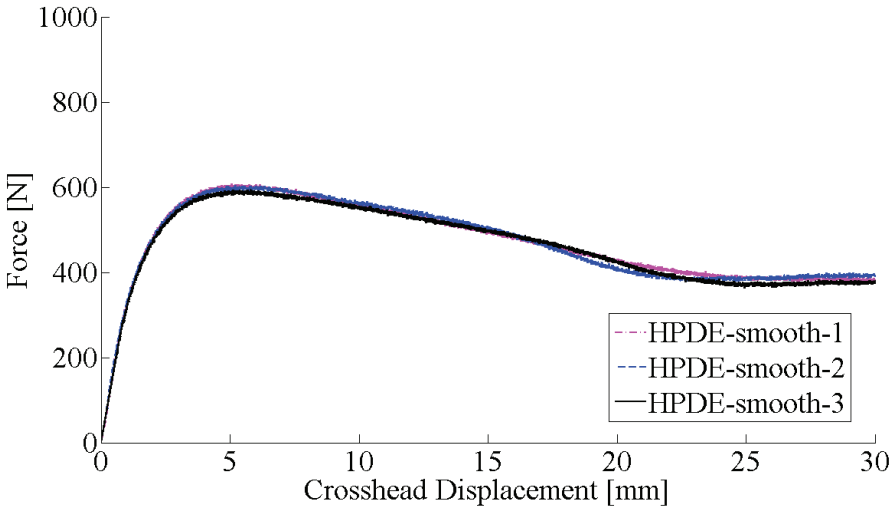

Comments: The smooth specimens in the tests fractured differently than expected. It seemed as the fractures developed along a spiral pattern on the outside of the specimens, and since this happened to all the smooth specimens it is assumed to be an effect from the machining. Some of the results from the smooth specimens may therefore be incorrect. The specimens did not fracture.

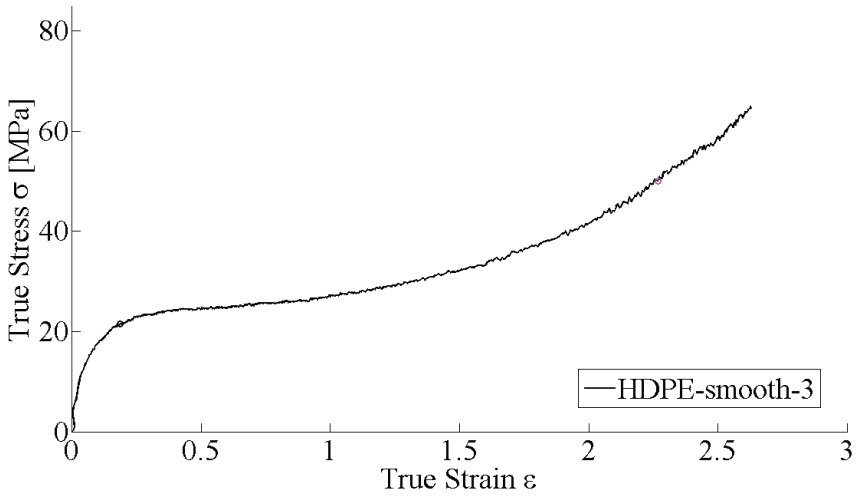
True Stress σ [MPa]
True Strain ε
HDPE-smooth-3
0
20
40
60
80
0
0.5
1
1.5
2
2.5
3

PVC_R08

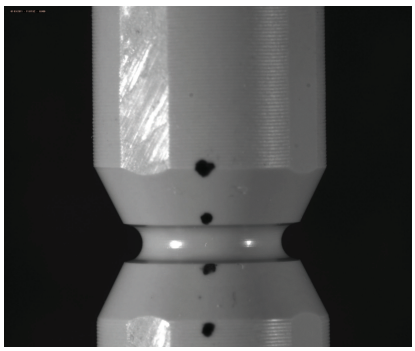

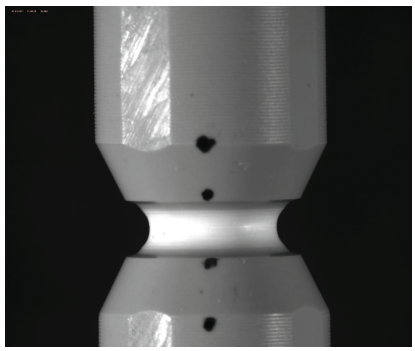

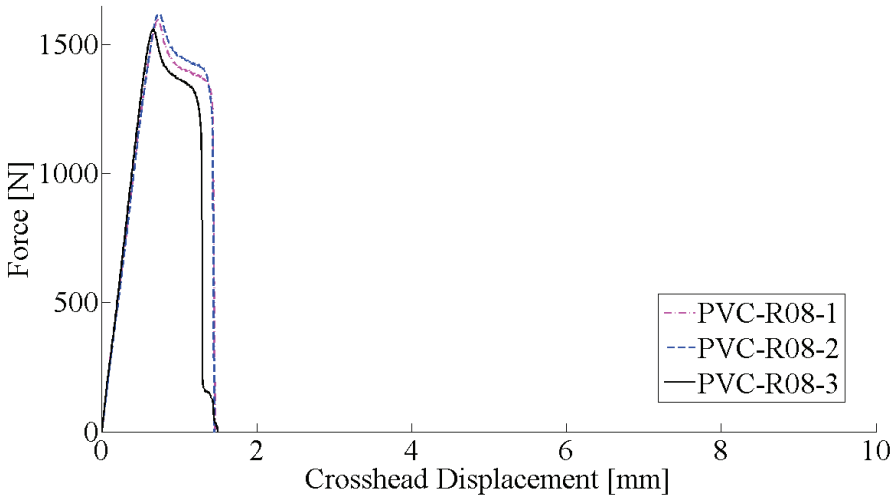
1500
1000
500
0
Force [N]
0
2
4
6
8
10
Crosshead Displacement [mm]
PVC-R08-1
PVC-R08-2
PVC-R08-3

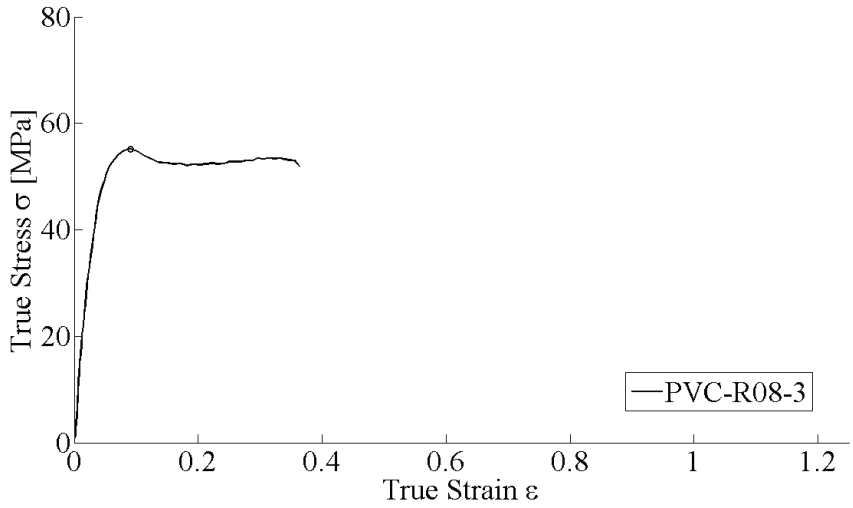

D_0	$6.00\,mm$
$D_\perp$	$5.48\,mm$
$D_\parallel$	$5.48\,mm$

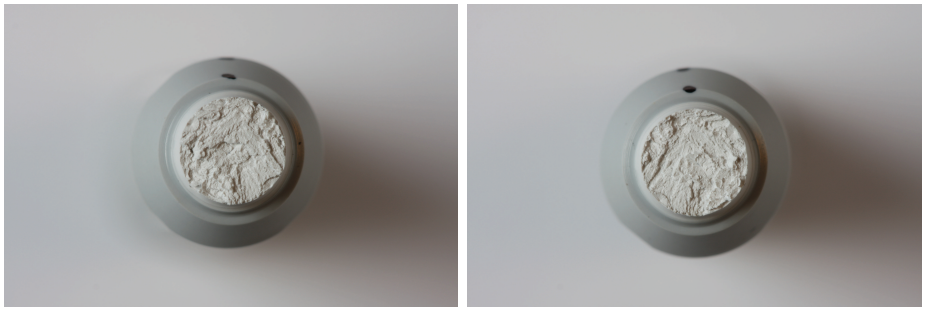

PVC_R2

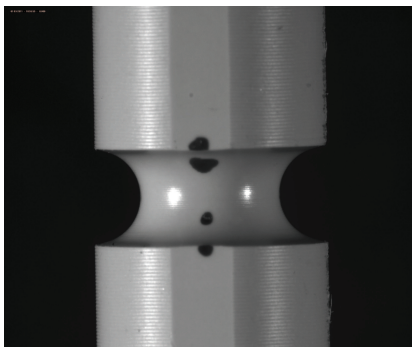

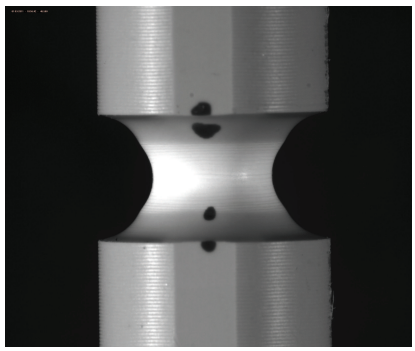

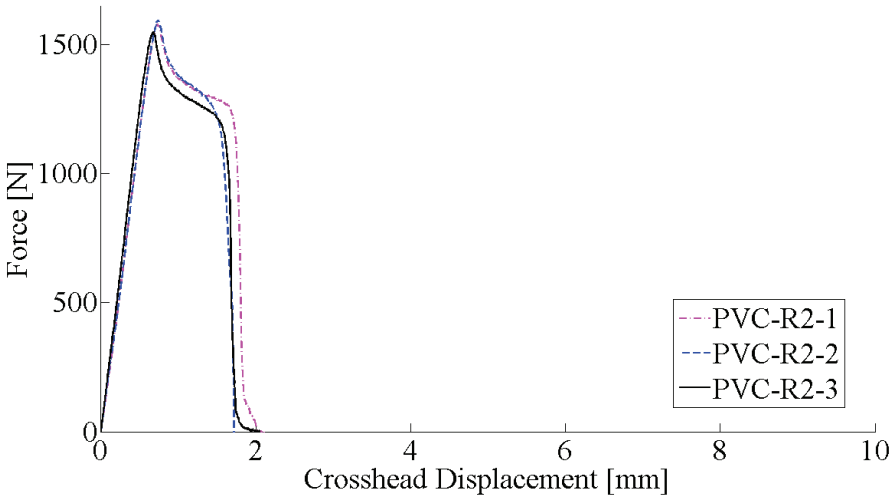
1500
1000
500
0
Force [N]
0
2
4
6
8
10
Crosshead Displacement [mm]
PVC-R2-1
PVC-R2-2
PVC-R2-3

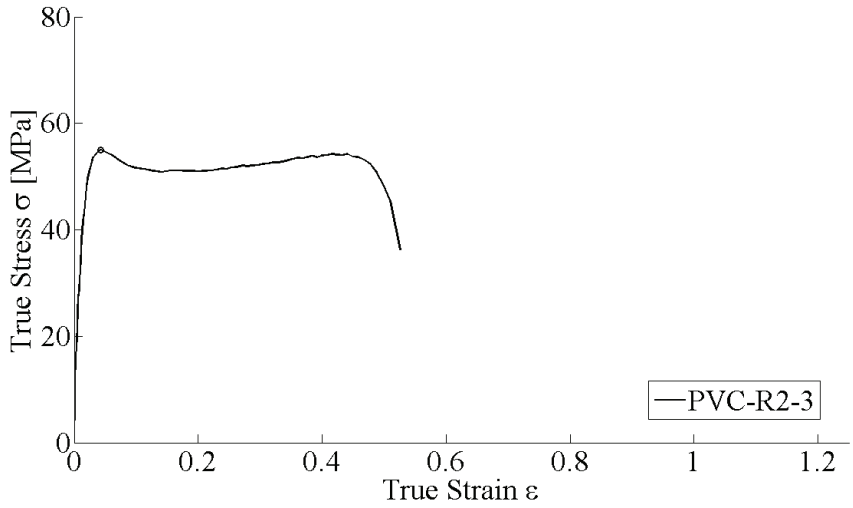

D_0	$5.98\,mm$
$D_\perp$	$5.25\,mm$
$D_\parallel$	$5.19\,mm$

PVC_R5

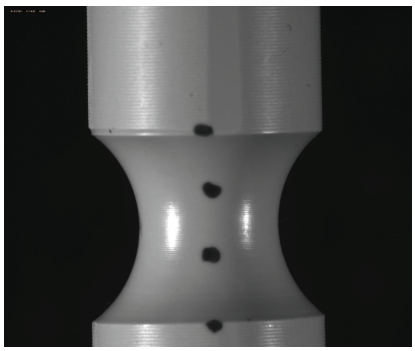

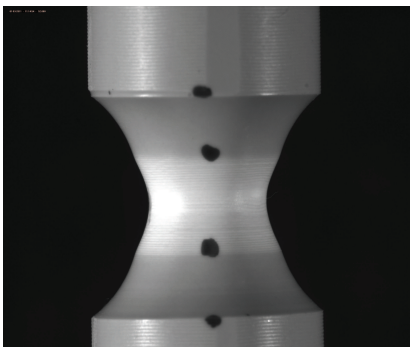

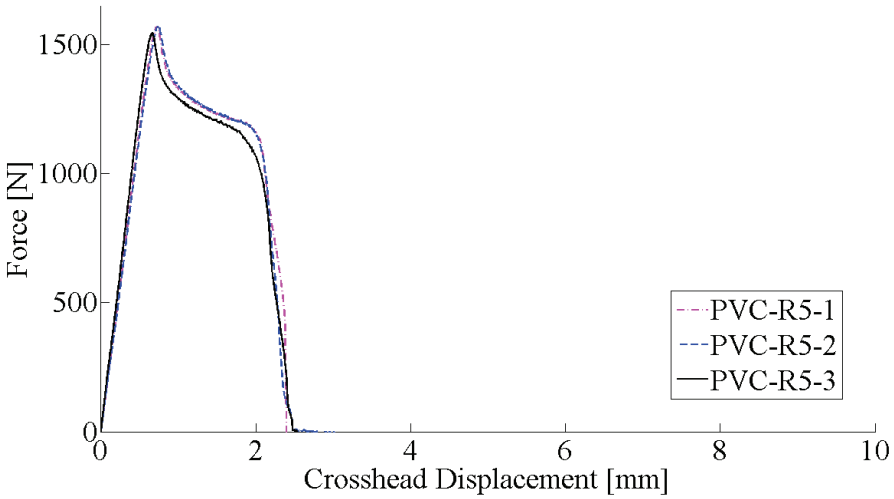
1500
1000
500
0
Force [N]
0
2
4
6
8
10
Crosshead Displacement [mm]
PVC-R5-1
PVC-R5-2
PVC-R5-3

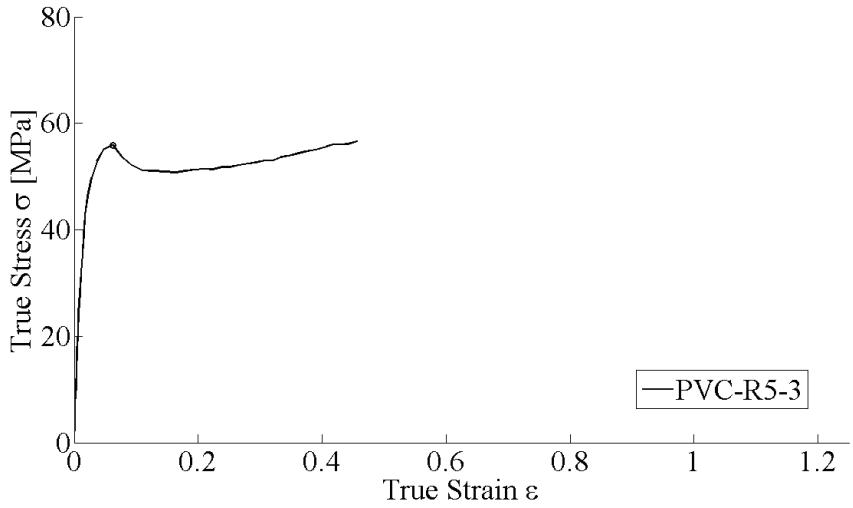

D_0	$5.99\,mm$
$D_\perp$	$4.78\,mm$
$D_\parallel$	$4.85\,mm$

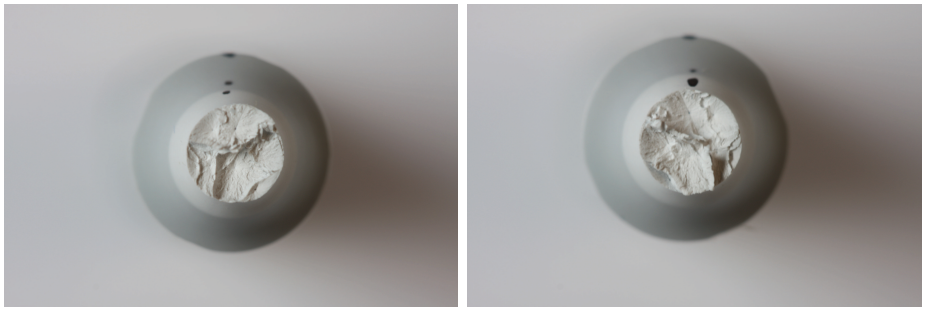

PVC_R20

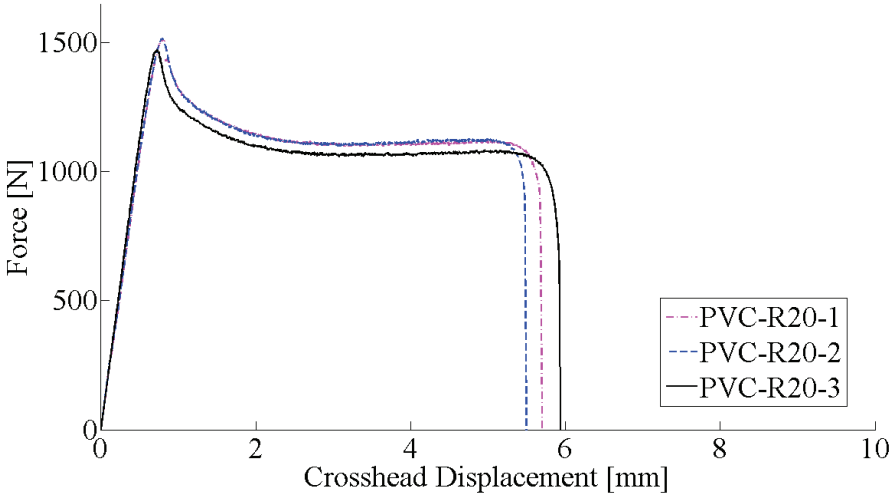
1500
1000
500
0
Force [N]
0
2
4
6
8
10
Crosshead Displacement [mm]
PVC-R20-1
PVC-R20-2
PVC-R20-3

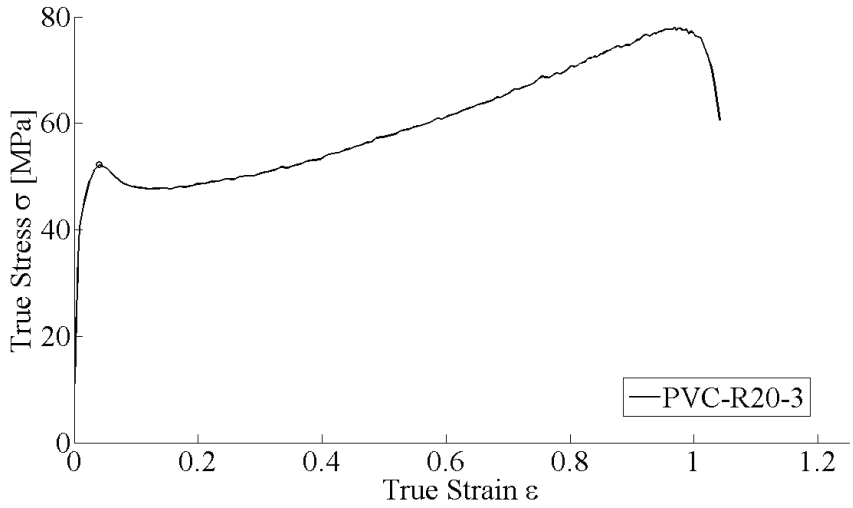

D_0	$6.03\,mm$
$D_\perp$	$4.31\,mm$
$D_\parallel$	$4.31\,mm$

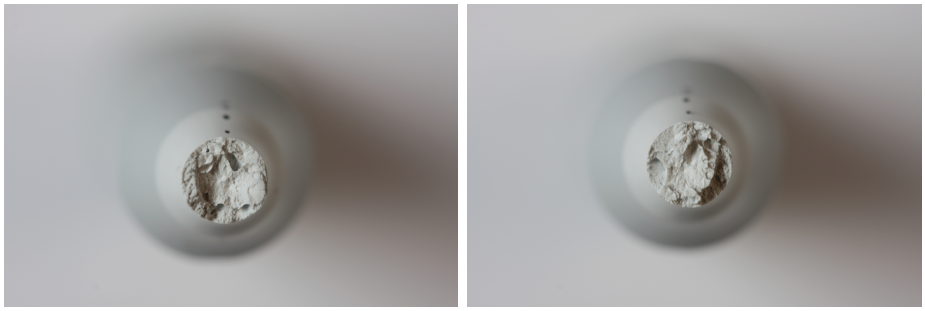

PVC_smooth

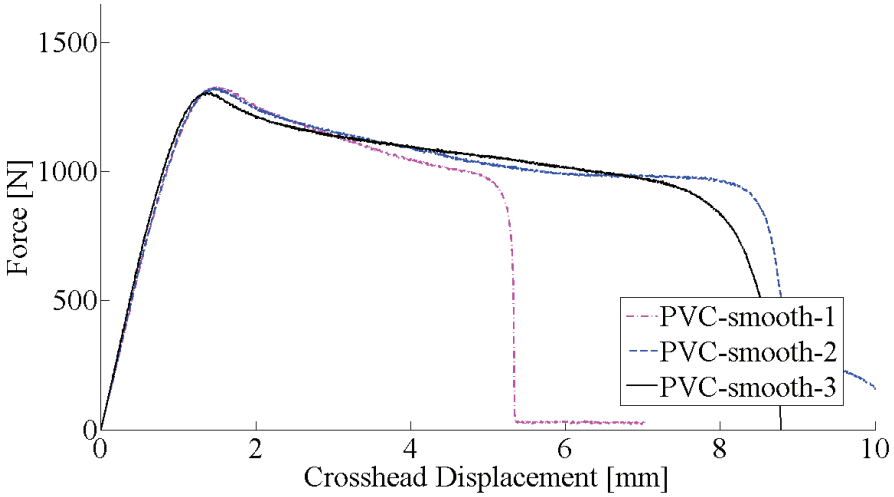

Comments: The smooth specimens in the tests fractured differently than expected. It seemed as the fractures developed along a spiral pattern on the outside of the specimens, and since this happened to all the smooth specimens it is assumed to be an effect from the machining. Some of the results from the smooth specimens may therefore be incorrect.

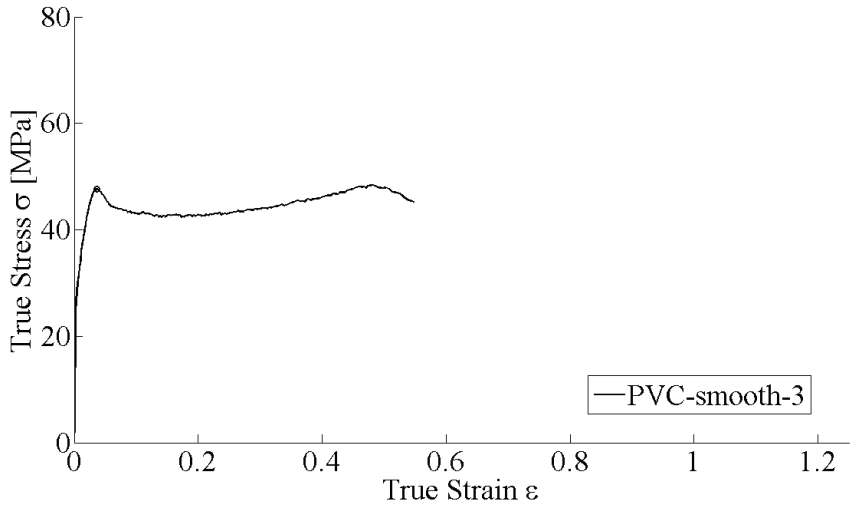

D_0	$5.99 mm$
$D_\perp$	$4.82 mm$
$D_\parallel$	$4.52 mm$

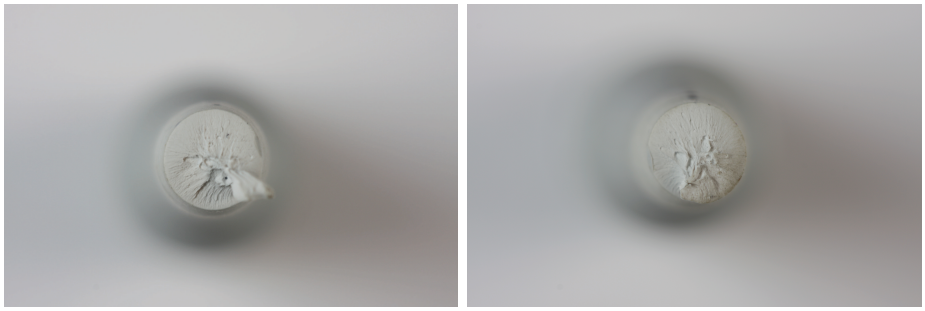

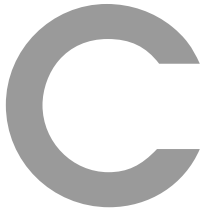

C

Appendix C

Representative LS-DYNA Keyword File from Tests

```
$$$$$$$$$$$$$$$$$$$$$$$$$$$$$$$$$$$$$$$$$$$$$$$$$$$$$$$$$$$$$$$$$$$$$$$$$$$$$$$$
$#             LS-DYNA Keyword file created by LS-PREPOST 3.0                  $
$                                   PVC_R2                                      $
$$$$$$$$$$$$$$$$$$$$$$$$$$$$$$$$$$$$$$$$$$$$$$$$$$$$$$$$$$$$$$$$$$$$$$$$$$$$$$$$

*KEYWORD

$$$$$$$$$$$$$$$$$$$$$$$$$$$$$$$$$$$$$$$$$$$$$$$$$$$$$$$$$$$$$$$$$$$$$$$$$$$$$$$$
$                              Control Options                                 $
$$$$$$$$$$$$$$$$$$$$$$$$$$$$$$$$$$$$$$$$$$$$$$$$$$$$$$$$$$$$$$$$$$$$$$$$$$$$$$$$

*CONTROL_CPU
$#  cputim
1.0000E+10
*CONTROL_DAMPING
$#  nrcyck     drtol    drfctr    drterm    tssfdr    irelal     edttl    idrflg
         0     0.000     0.000     0.000     0.000         0     0.000         0
*CONTROL_ENERGY
$#    hgen      rwen    slnten     rylen
         2         2         2         2
*CONTROL_OUTPUT
$#   npopt    neecho    nrefup    iaccop     opifs    ipnint    ikedit    iflush
         0         0         0         0     0.000         0         0         0
$#   iprtf    ierode     tet10    msgmax    ipcurv
         0         0         2        50         0
*CONTROL_SOLID
```

```
$#   esort    fmatrix    niptets     swlocl     psfail
         1          0          4          2          0
$#    pm1       pm2       pm3       pm4       pm5       pm6       pm7       pm8       pm9      pm10
       0         0         0         0         0         0         0         0         0         0
*CONTROL_TERMINATION
$#  endtim     endcyc      dtmin     endeng     endmas
 67.000000          0      0.000      0.000      0.000
*CONTROL_TIMESTEP
$#  dtinit     tssfac       isdo     tslimt      dt2ms       lctm      erode      ms1st
     0.000      0.000          0      0.000      0.000          0          0          0
$#  dt2msf    dt2mslc      imscl
     0.000          0          0


$$$$$$$$$$$$$$$$$$$$$$$$$$$$$$$$$$$$$$$$$$$$$$$$$$$$$$$$$$$$$$$$$$$$$$$$$$$$$$$$$$$$$$$$$$$$$$$$$$$$
$                                   Database Options                                              $
$$$$$$$$$$$$$$$$$$$$$$$$$$$$$$$$$$$$$$$$$$$$$$$$$$$$$$$$$$$$$$$$$$$$$$$$$$$$$$$$$$$$$$$$$$$$$$$$$$$$

*DATABASE_GLSTAT
$#      dt    binary      lcur     ioopt
  0.500000         0         0         1
*DATABASE_SECFORC
$#      dt    binary      lcur     ioopt
  0.500000         1         0         1
*DATABASE_BINARY_D3PLOT
$#      dt      lcdt      beam     npltc    psetid
  0.500000         0         0         0         0
$#   ioopt
         0
*DATABASE_CROSS_SECTION_PLANE_ID
$#     csid                                                                                title
         1
$#     psid       xct       yct       zct       xch       ych       zch    radius
         0 -0.975448-43.654499  4.903930 -0.975448-21.684500  4.903930     0.000
$#     xhev      yhev      zhev      lenl      lenm        id     itype
     0.000     0.000     0.000     0.000     0.000         0         0


$$$$$$$$$$$$$$$$$$$$$$$$$$$$$$$$$$$$$$$$$$$$$$$$$$$$$$$$$$$$$$$$$$$$$$$$$$$$$$$$$$$$$$$$$$$$$$$$$$$$
$                                   Material Definitions                                          $
$$$$$$$$$$$$$$$$$$$$$$$$$$$$$$$$$$$$$$$$$$$$$$$$$$$$$$$$$$$$$$$$$$$$$$$$$$$$$$$$$$$$$$$$$$$$$$$$$$$$

*MAT_USER_DEFINED_MATERIAL_MODELS
$      MID       rho      User mat #     LMC     # Hist var              IBULK        IG
$#     mid        ro            mt       lmc          nhv     iortho     ibulk        ig
         1 1.430E-3            48        16           50          0        15        16
$---+---1---+---2---+---3---+---4---+---5---+---6---+---7---+---8
$       IVECT      IFAIL     ITHERM    IHYPER       IEOS
$#   ivect      ifail     itherm     ihyper       ieos
```

```
          0         0         0         1         0
$---+---1---+---2---+---3---+---4---+---5---+---6---+---7---+---8
$   E         Poisson      eps0         C    sigma_T        Cr N (lamda_L)     alfa
$#      p1        p2        p3        p4        p5        p6        p7        p8
 3000.0000  0.300000  0.001000  0.070000 46.800000  6.070000  1.710000  1.300000
$---+---1---+---2---+---3---+---4---+---5---+---6---+---7---+---8
$   beta        kappa     sigma_ss     H                              K         G
$#      p1        p2        p3        p4        p5        p6        p7        p8
  1.270000     0.000 37.800000 15.000000     0.000     0.000 2500.0000 2142.0000


$$$$$$$$$$$$$$$$$$$$$$$$$$$$$$$$$$$$$$$$$$$$$$$$$$$$$$$$$$$$$$$$$$$$$$$$$$$$$$$$$$$
$                                   Part Definitions                                 $
$$$$$$$$$$$$$$$$$$$$$$$$$$$$$$$$$$$$$$$$$$$$$$$$$$$$$$$$$$$$$$$$$$$$$$$$$$$$$$$$$$$

*PART
$# title

$#     pid     secid       mid     eosid      hgid      grav    adpopt      tmid
         1         1         1         0         1         0         0         0
*HOURGLASS
$#    hgid       ihq        qm       ibq        q1        q2    qb/vdc        qw
         1         5     0.000         0     0.000     0.000     0.000     0.000


$$$$$$$$$$$$$$$$$$$$$$$$$$$$$$$$$$$$$$$$$$$$$$$$$$$$$$$$$$$$$$$$$$$$$$$$$$$$$$$$$$$
$                                  Section Definitions                               $
$$$$$$$$$$$$$$$$$$$$$$$$$$$$$$$$$$$$$$$$$$$$$$$$$$$$$$$$$$$$$$$$$$$$$$$$$$$$$$$$$$$

*SECTION_SOLID
$#    secid     elform        aet
         1         1         0
*SET_SOLID
$#      sid     solver
        1MECH
$#       k1        k2        k3        k4        k5        k6        k7        k8
*ELEMENT_SOLID
$#    eid       pid        n1        n2        n3        n4        n5        n6        n7        n8
*NODE
$#    nid               x                 y                 z        tc        rc


$$$$$$$$$$$$$$$$$$$$$$$$$$$$$$$$$$$$$$$$$$$$$$$$$$$$$$$$$$$$$$$$$$$$$$$$$$$$$$$$$$$
$                                     Load Curve                                     $
$$$$$$$$$$$$$$$$$$$$$$$$$$$$$$$$$$$$$$$$$$$$$$$$$$$$$$$$$$$$$$$$$$$$$$$$$$$$$$$$$$$
*DEFINE_CURVE_SMOOTH
$#     lcid      sidr      dist     tstart      tend     trise        v0
         1         0  2.080000 1.0000E-5 67.000000  0.020000     0.000
```

```
$$$$$$$$$$$$$$$$$$$$$$$$$$$$$$$$$$$$$$$$$$$$$$$$$$$$$$$$$$$$$$$$$$$$$$$$$$$$$$$$
$                                  Node Sets                                   $
$$$$$$$$$$$$$$$$$$$$$$$$$$$$$$$$$$$$$$$$$$$$$$$$$$$$$$$$$$$$$$$$$$$$$$$$$$$$$$$$

*SET_NODE_LIST_TITLE
moving
         1     0.000     0.000     0.000     0.000MECH

     50441     50442     50443         0         0         0         0         0
*SET_NODE_LIST_TITLE
fixed
         2     0.000     0.000     0.000     0.000MECH


$$$$$$$$$$$$$$$$$$$$$$$$$$$$$$$$$$$$$$$$$$$$$$$$$$$$$$$$$$$$$$$$$$$$$$$$$$$$$$$$
$                              Boundary Conditions                             $
$$$$$$$$$$$$$$$$$$$$$$$$$$$$$$$$$$$$$$$$$$$$$$$$$$$$$$$$$$$$$$$$$$$$$$$$$$$$$$$$

*BOUNDARY_PRESCRIBED_MOTION_SET
         1         2         0         1  1.000000         01.0000E+28     0.000
*BOUNDARY_SPC_SET
         1         0         1         0         1         1         1         1
*BOUNDARY_SPC_SET
         2         0         1         1         1         1         1         1


*END
*COMPONENT
         1  0.769000  0.004000  0.110000     0.000         0         0         0
Part 1
*COMPONENT_PART
         1         1
*COMPONENT_END
```